Transient Modeling Tool for the Counterflow Heat Exchangers in Concentrating Solar Power Systems with Thermal Energy Storage

by

Samuel Springate

A thesis submitted in partial fulfilment of

the requirements for the degree of

Master of Science

(Mechanical Engineering)

at the

UNIVERSITY OF WISCONSIN – MADISON

December 22, 2021

Acknowledgements

In the summer of 2020, I made the decision to come to the University of Wisconsin-Madison to pursue my MS in Mechanical Engineering. From my first day in this wonderful city, I have come to love Madison and the people here. But most importantly, I have had so many opportunities to expand my technical knowledge and engross myself in graduate research with the Energy Systems Optimization and Solar Energy Lab. It has been a pleasure to work with Dr. Greg Nellis and Dr. Mike Wagner during my time at UW-Madison. I cannot say enough good things about them – with their vast technical knowledge, I always have a resource when I have complex questions, and they have done a fantastic job with learning how to problem solve by asking the important questions to discover the answers myself. Working in this group and getting to know the talented students and faculty associated with the lab has been a lot of fun and has provided me with the perfect stepping-stone into my career moving forward. I have not told Greg this, but during the first interview I had with a company in California, the engineering manager told me he had Greg's Heat Transfer textbook sitting on his desk as we spoke.

I also had the opportunity to be involved with the Energy Analysis and Policy Graduate Certificate program at UW-Madison. This program is geared towards individuals in multiple disciplines looking to be involved in the inconceivably large problems in energy that we face today. This has given me the opportunity to network with some incredible people that have taught me so much. Between the intriguing coursework and weekly seminars, I am constantly learning about the wonderful ways so many people are tackling our ongoing climate struggle.

Lastly, thank you to my family and friends that have been there for me along the way. My parents have been so supportive during my time at UW-Madison, and I am so grateful for them that I am seriously at a loss for words. Finally, thank you to all my friends that have been a part of this, but thank you especially to the friends I have come to know in Madison that have made this experience so much easier.

Abstract

Concentrating solar power systems present a significant low-carbon opportunity for large-scale inexpensive energy storage and grid stabilization. Traditionally, renewable energy technologies provide little support to reliable power generation. However, utility-scale concentrating solar power systems with thermal energy storage capacity are highly suited to combat the increasing need for electricity. This promising technology, especially when used in conjunction with other power generation methods, supports high loads during peak hours. Dispatchable energy systems provide this critical support to the grid, especially in high-penetration renewable electricity markets. The full capabilities of these systems are being experimented with in hybrid power plants, utilizing the full capacity of multiple technologies to support one another. Because of the unique application of these systems, it is crucial to maximize revenue through the sale of this high-value electricity and therefore, by maximizing the cycle performance, as well.

A high-temperature power cycle, such as that in a solar a thermal power plant, is characterized by one or more costly heat exchangers. The transient response of the power plant during non-steady conditions such as load changes and cycle start-up is not instantaneous; therefore, it is important to gain a better understanding of the characterization of the heat exchangers. This thesis outlines a transient numerical model that has been implemented in MATLAB providing improved visualization of counterflow recuperative heat exchangers within an operating power cycle undergoing transient conditions using common inputs, and the effects of that behavior may lead to a better understanding of the effects on other cycle componentry. This model has been verified against multiple types of transient simulations from different authors in addition to verification against the conventional effectiveness-NTU model at steady-state.

While much of this study focuses on the supercritical carbon dioxide Brayton cycle – a promising power conversion technology that is relevant to applications such as nuclear power, concentrating solar thermal, fossil fuel boilers, and shipboard propulsion systems – the model is not limited to a particular type of cycle. This flexible model enables the user to provide inputs to derive meaningful results describing the transient response of any type of counterflow heat exchanger – including recuperators, regenerators, boilers, precoolers, and intercoolers.

Contents

List of Figures

List of Tables

Nomenclature

Abbreviations

CSP	Concentrating Solar Power	[-]
sCO2	Supercritical Carbon Dioxide	[-]
eff-NTU	Effectiveness NTU	[-]

Terminology

T	Temperature	[K]
β_T	Temperature ramp rate	[K/s]
$\beta_{\dot{C}}$	Capacitance rate ramp rate	[W/K-s]
$\dot{C}$	Capacitance rate of fluid	[W/K]
$\bar{C}$	Cold fluid fixed capacity [2]	[J/K]
UA	Overall thermal conductance	[W/K]
C_{tot}	Total heat capacity of metal wall	[J/K]
$T_{m,ini}$	Initial metal node temperatures	[K]
R	Resistance	[K/W]
$R_{cond,tot}$	Total axial conduction resistance of metal wall	[K/W]
R_{cond}	Axial conduction resistance of metal wall per node	[K/W]
R_h	Hot fluid convection resistance [2]	[K/W]
R_c	Cold fluid convection resistance [2]	[K/W]
L	Length for conduction	[m]
N	Number of nodes	[-]

M	Number of timesteps	[-]
θ	Time [2]	[s]
θ_d	Dwell time [2]	[s]
θ_d^*	Dimensionless dwell-time ratio [2]	[-]
θ^*	Dimensionless time parameter, time relative to dwell time [2]	[-]
R^*	Relative resistance ratio [2]	[-]
$\bar{C}_w^*$	Dimensionless wall capacity relative to fluid capacity [2]	[-]
C_R	Capacitance ratio	[-]
ε_f^*	Dimensionless effectiveness ratio	[-]
ε_f	Fluid effectiveness	[-]
ε_{fss}	Fluid effectiveness at steady-state	[-]
$\dot{q}$	Heat transfer rate	[W/K]
x	x-axis parameter	[-]
y	y-axis parameter	[-]
t_{ramp}	Ramp time	[s]
t_{sim}	Simulation time	[s]
t_{span}	Integration time span	[s]
τ	Time constant	[s]
x^*	Non-dimensionalized position parameter	[-]

Subscripts

min	Minimum	[-]
max	Maximum	[-]

in	Inlet	[-]
ini	Initial	[-]
fin	Final	[-]
f	Fluid	[-]
h	Hot fluid	[-]
c	Cold fluid	[-]
m	Metal wall	[-]
w	Metal wall [2]	[-]
$conv$	Convection	[-]
$cond$	Conduction	[-]
tot	Total	[-]
ss	Steady-state	[-]

1 Background

Concentrating solar power (CSP) is an emerging power generation technology that produces electricity from the sun. While many people would primarily consider photovoltaics when thinking about solar energy, CSP is actually quite different. Traditional photovoltaic solar energy utilizes solar radiation to generate an electric current in certain photoelectric materials – converting sunlight directly into electricity. For most photovoltaic panels, this reaction occurs at fairly low temperature ranges compared to temperatures achieved in CSP and is entirely dependent on the current availability of sunlight. While utility-scale solar photovoltaic power plants can contribute electricity to support peak demand during the day-time hours, there is no intrinsic ability to store power and release it to the grid on demand. Even with batteries and other storage technologies, there is relatively little potential to store power with photovoltaics. This is one of the many reasons why CSP provides a more stable form of solar power generation – allowing for the possibility to provide power to the grid regardless of the time of day.

In a CSP plant, solar radiation is redirected using mirrors towards a central receiver capable of absorbing concentrated flux. Many types of such receivers exist, but for simplicity, this description will focus on the molten salt power tower configuration displayed in **Figure 1**.

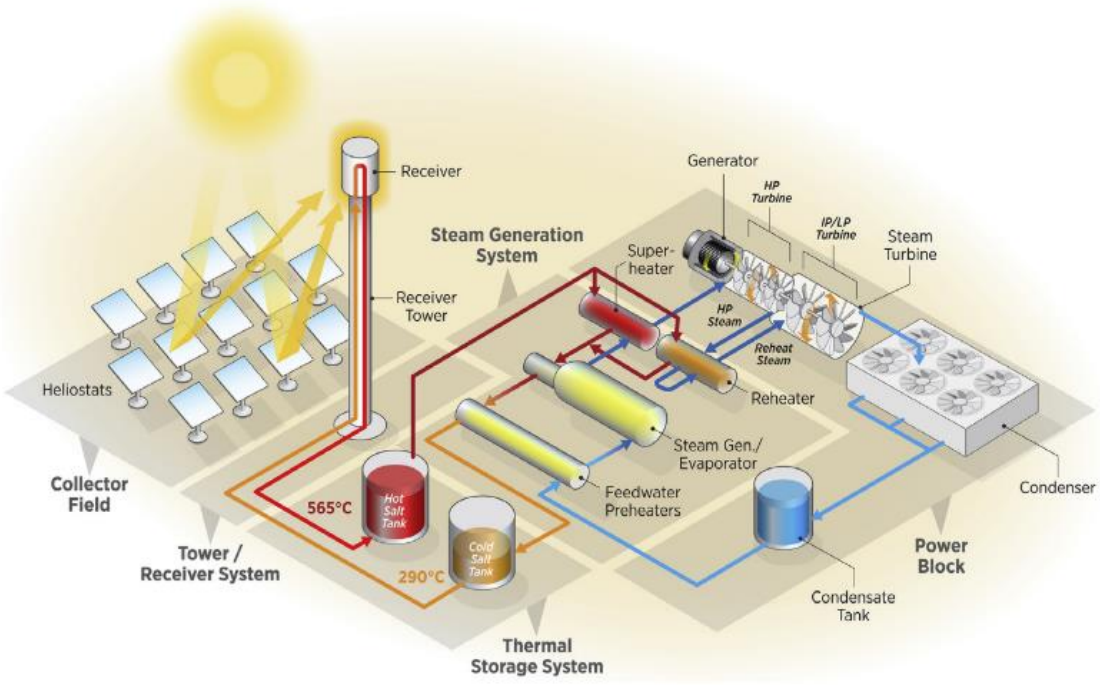

Figure 1. Molten Salt Power Tower CSP configuration [7].

In this configuration, a molten nitrate salt flows through piping in direct contact with the receiver tubing. Molten salt has a large enough heat capacity to absorb significant amounts of heat that may be subsequently stored in a tank or immediately used to generate steam. If the molten salt is used to immediately produce steam, then it will flow through the steam generation system to power a steam turbine producing useful electricity. Then, the molten salt will flow back towards the receiver to once again be heated, and the cycle repeats.

One of the many advantages of CSP is the significant thermal energy potential that may be stored for use at a later time, such as when the grid reaches maximum demand. At times like these, the thermal energy storage tank can be depleted as necessary to provide electricity via steam generation as previously discussed. This form of power plant, which can be turned on and off as necessary, refers to an electrical power system that provides dispatchable electricity to the grid.

Being able to provide stable electricity to the grid regardless of minor disruptions in weather patterns is appealing when compared to the traditional solar photovoltaic power generation. In some cases, it is practical to combine these technologies into a combined power plant, with utility-scale photovoltaics, to maximize utilization of solar energy. One example of this may be done with utility-scale photovoltaics as shown in **Figure 2**.

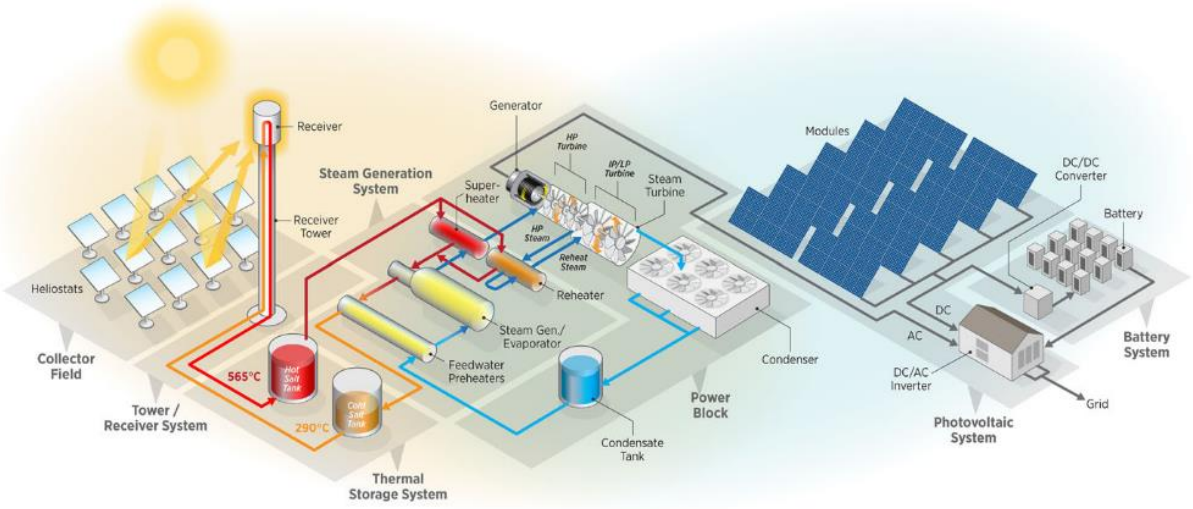

Figure 2. CSP Thermal Energy Storage Photovoltaic hybrid system configuration [8].

There is significant research being conducted to improve the overall efficiency and decrease the costs of CSP plants, but this thesis will focus on the Brayton cycle, specifically the recuperative heat exchangers. The supercritical carbon dioxide (sCO2) Brayton cycle is a promising power conversion technology that is relevant to applications such as nuclear power, concentrated solar thermal, fossil fuel boilers, and shipboard propulsion systems [4].

1.1 The Brayton Cycle

Many types of performance-enhancing mechanisms are used in a modified Brayton cycle, but this study focuses broadly on the recuperative heat exchangers in this cycle.

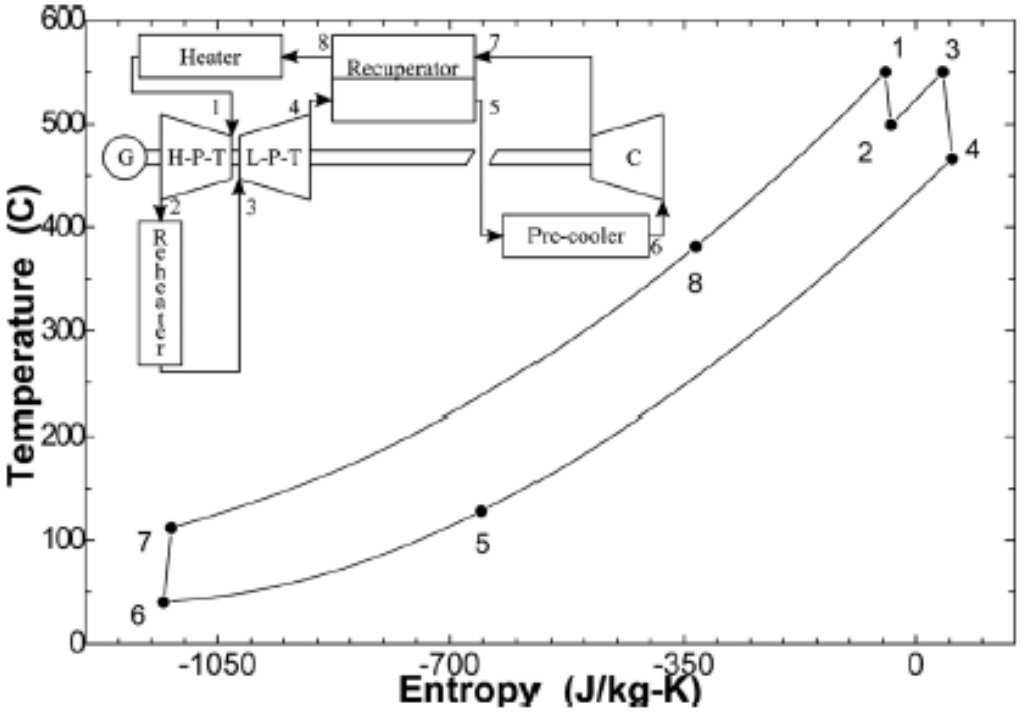

Figure 3. Graph of simple Brayton Cycle with reheat [1].

More complex cycles are often developed from the simple recuperative Brayton cycle shown in **Figure 3**. For the specified sCO2 process, high-pressure sCO2 exits the compressor and enters the recuperator as the cold flow (7). Low-pressure sCO2 exits the low-pressure turbine and enters the recuperator as the hot flow (4). The hot stream transfers energy to the cold stream and exits to the precooler (5), where the compressor inlet temperature (6) is reached by rejecting energy to the cold sink. The cold flow increases in temperature in the recuperator and exits to the heater (8), where the external heater provides heat to the fluid before the high-pressure turbine inlet (1). With reheat, the fluid exits the high-pressure turbine at (2), then the fluid passes through the reheater and low-pressure turbine (3) before entering the recuperator [1]. For improved cycle efficiency, modifications are made to the simple recuperative Brayton cycle by adding re-compression and another recuperator as shown in **Figure 4**. The primary goal of this

recompression cycle is to reduce the pinch point effect occurring in the cycle with a single recuperator, which is caused by the difference in the fluid capacitance rates [1].

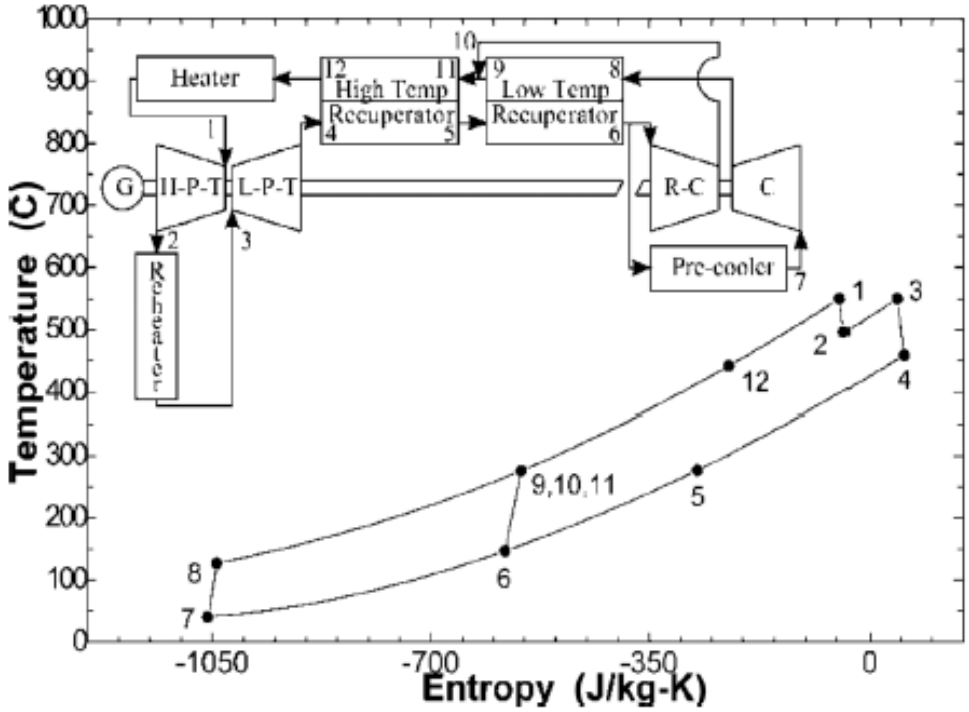

Figure 4. Graph of recompression Brayton cycle with reheat [1].

1.2 Heat Exchanger Analysis

For any heat exchanger, the fundamental goal is to transfer heat from a hot fluid to a cold fluid. This can be done in many types of ways in various configurations. The main configuration types are parallel-flow, counter-flow, cross-flow, and shell-and-tube.

In a counterflow heat exchanger, the basic idea is for a cold fluid to enter one side of the heat exchanger at the cold inlet and for a hot fluid to enter the other side of the heat exchanger at the hot inlet – where the hot and cold fluids flow in opposite, parallel directions. These fluids are unmixed with one another. Heat can be transferred through a plate separating flows in

rectangular ducts or across circular pipes. Sometimes it is the case that the thermal resistance of the plate or tube walls is insignificant and therefore, likely thin, since thermal resistance is directly proportional to the conduction length through a material. However, it is possible for there to be a significant storage term in the metal due to the heat capacity and time rate of change of the fluids, as well, that may affect the rate of heat transfer. If the rate of change of the fluid is greater than the lumped capacitance time constant of the metal, for example, the thermal capacitance of the metal becomes important. Because of this storage term in the metal, the hot flow is not transferring heat completely to the cold fluid prior to the metal reaching a steady temperature. This means there is an unsteady transfer of heat or a non-constant flow of energy when the heat exchanger is undergoing transient conditions. This rate of heat transfer can be calculated as a function of time to find the value at any point in time. After some time, the transient effects become less significant, and the system will reach steady-state. This means there is a constant rate of heat transfer between the fluids until extraneous inputs are introduced to the system or the constant inputs change value.

When attempting to solve a transient heat exchanger problem, the most common required inputs are the fluid inlet temperatures, fluid inlet pressures, fluid capacitance rates, conduction resistance in the metal, convective resistances at the surface, total heat capacity of the metal, and the initial temperature of the plate. This allows for a system of equations to be created to numerically simulate the response of the heat exchanger. The purpose of the recuperative heat exchangers in high-temperature CSP systems is to increase the temperature of the cold fluid as it passes through the heat exchanger. This accomplishes four goals: (i) increasing the average temperature of heat addition to the cycle while allowing for compression in a region of high fluid

density, (ii) utilizing heat in the hot fluid that would have otherwise been rejected, (iii) minimizing the amount of work that must be done by the heater in the following step of the Brayton cycle, and (iv) maximizing the amount of heat transfer from the hot fluid to the cold fluid.

1.3 Motivation

The overarching goal of this effort is to create a flexible counterflow heat exchanger model that can handle a broad set of inputs for many types of situations – like in the Brayton cycle for high-temperature power cycles such as molten salt power tower CSP systems. This model will capture the effects of transient behavior in the heat exchanger metal. The following section discusses existing transient models that look at highly complex configurations and models that use results from electromechanical analog tests to mimic numerical simulations. The goal of the present work is to create a model that analyzes transient conditions in counterflow heat exchangers using common inputs.

2 Literature Review

This section discusses existing work in counterflow heat exchanger modeling for concentrating solar power and various types of transient modeling for other applications.

2.1 The Transient Response of Gas-Turbine-Plant Heat Exchangers [2]

This report summarizes the transient response of gas-turbine-plant heat exchangers in graphical form and is supplemented with additional results from analytical solutions and electromechanical analog tests. An analytical model of a counterflow heat exchanger is examined for several cases: the regenerator, intercooler, precooler, and insulated duct. When the analytical solution is not possible due to limiting cases, the electromechanical analog test results are provided in addition to the analytical solution. This work also examines the effect of various non-dimensional parameters on the effectiveness of the heat exchanger. The most significant parameters relate fluid capacitance ratios, wall-to-fluid capacity ratios, time, and position in the heat exchanger. This study provides a table of solutions for several types of solutions based on inputs and constraints – some of which are analyzed in Chapter 3.

2.2 Transient Modeling using Numerical Propulsion System Simulation (NPSS) [3]

This source examines a transient model of a 10 MW sCO2 Brayton power cycle using NPSS. The mode includes a compressor, turbine, recuperator, cooler, heater, pipes, and valves. This model neglects axial conduction through the walls unlike the model described in this thesis. However, this model does real data calculations for the fluids in the heat exchanger. This software platform simulates the transient responses of sCO2 power cycles due to three primary attributions: (i) ability to only use a single software platform for the entire model, (ii) NPSS has proven solvers

for both steady-state and transient solutions, and (iii) the flexibility to include an extensive library of fluid properties to solve complicated systems. Researchers have been using the NPSS platform to develop transient simulations for open-loop air Brayton cycles [3]. The study goes on to analyze methods for ramping down in practical operation. This type of software requires many inputs that may not necessarily be known in the case of the model this thesis focuses on. While this software has many capabilities and implements a robust solver, it is not always necessary to perform such a detailed analysis for the transient response in a counterflow heat exchanger.

2.3 Development and Verification of Transient Analysis Tool using sCO2 Brayton Cycle [4]

This paper compares experimental data against results from SCTRAN/CO2 transient simulations – primarily for nuclear applications. The main schematic map details a nuclear reactor system cooled by the sCO2 Brayton cycle. In these applications, the high-temperature sCO2 flows into the gas turbine and drives shaft rotation which produces electricity when connected to a generator [4]. The transient analysis code can simulate the reactor core, precooler, recuperator, and turbomachinery components such as the compressor, gas turbine, and rotating shaft model [4]. SCTRAN is a one-dimensional safety analysis code for supercritical water reactors. The homogeneous fluid flow model assumes the two phases of coolant are in thermal equilibrium and that there is no difference in velocity. Because the state of sCO2 remains in the gas state for this application, the homogeneous model is adopted to develop the transient analysis code for the sCO2 Brayton cycle [4]. This analysis examines the models for the compressor, gas turbine, shaft, and heat exchanger. By incorporating these models in addition to the thermal property data, heat transfer model, and friction model for carbon dioxide, a transient analysis code was created with SCTRAN/CO2. While this model is useful, much data about fluid properties and

turbomachinery performance is required. This makes this type of model highly specific and more difficult to use in cases where exact precision is not necessary.

2.4 Transient Response of the Counterflow Heat Exchanger [5]

This source analyzes the transient behavior of the temperatures of fluids leaving heat exchangers for process control applications. Because several previous papers summarize transient performance in counterflow heat exchangers restricted to gas-to-gas conditions, this paper looks at the case where the fluids are gases and liquids. The results are compared against results from London et. al for thermal-electric analog test results and analytical solutions that are like those found in London et. al [2]. By varying four parameters deemed to include many technical applications and using a finite difference method to solve, this source presents the responses to a unit step increase of both inlet temperatures. Because this source is quite old, it does not provide any useful transient analysis code and is useful in reference only.

3 Model Derivation

This section reviews the model, how it is derived, assumptions that are made and how they affect the breadth of applicability, and how the model performs against other models.

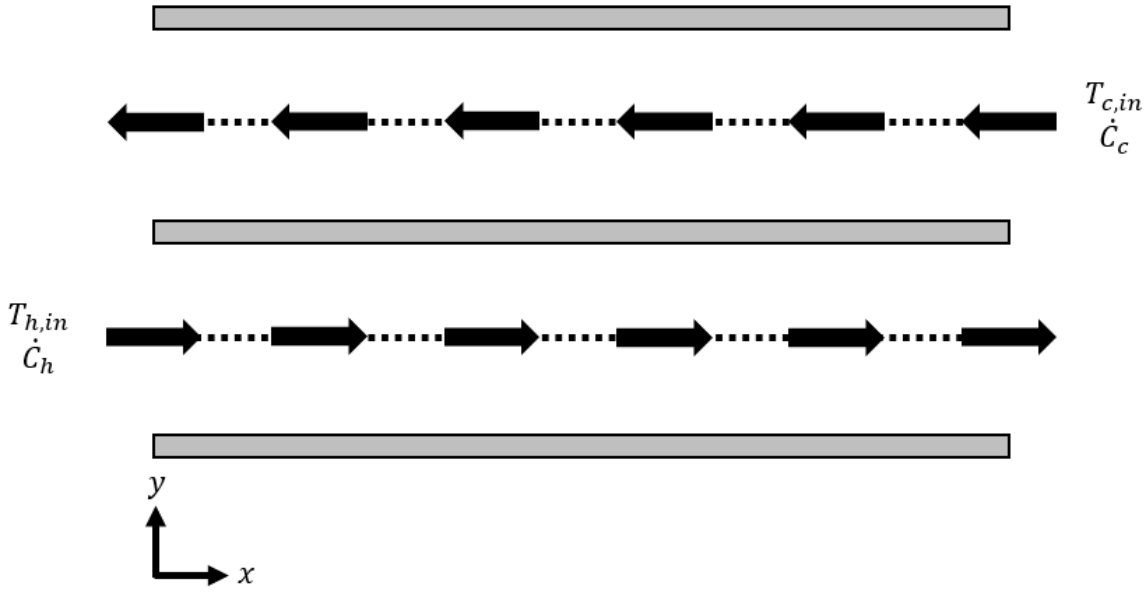

Figure 5. Basic schematic of counterflow heat exchanger flow.

3.1 Inputs & Assumptions

A working model has been created to fully understand the properties and characteristics of these recuperative heat exchangers given inputs in **Table 1**.

Table 1. Heat Exchanger Model Inputs

Property	Variable	Units
Hot inlet temperature	$T_{h,in}$	K
Cold inlet temperature	$T_{c,in}$	K
Hot fluid capacitance rate	$\dot{C}_h$	W/K
Cold fluid capacitance rate	$\dot{C}_c$	W/K
Hot fluid thermal conductance	UA_h	W/K
Cold fluid thermal conductance	UA_c	W/K
Total heat capacity of metal	C_{tot}	J/K
Total axial conduction resistance of metal	$R_{cond,tot}$	K/W
Initial metal node temperatures	$T_{m,ini}$	K

For this model, the temperature of the metal, T_m, is a function of time and the x-position in the axial direction and not a function of the y-position – this means that the temperature of the metal in the y-direction has a single value at each x-position. Another assumption this model makes is that the conductive resistance in the metal in the y-direction is small compared to the resistance to convection at the surface; therefore, this conductive resistance can be completely neglected. The fluid inlet temperatures, $T_{h,in}$ and $T_{c,in}$, and the fluid capacitance rates, $\dot{C}_c$ and $\dot{C}_h$, are a function of time, as well. The user will input these values as step inputs for a given number of timesteps. The thermal conductance, UA_h and UA_c, of the fluids are constants. These values can be used to calculate the overall thermal conductance, UA, of the heat exchanger, which is independent of geometry since the total conductance encompasses all resistances. The total heat capacity, C_{tot}, and the axial conductive resistance, $R_{cond,tot}$, of the metal are also constants – where both values are partitioned equally into $N-1$ values of individual heat capacities and axial conductive resistances, respectively, for each control volume between nodes.

3.2 Finding the Numerical Solution

The first step in finding the numerical solution for the model is to derive the state equations to be integrated numerically through the heat exchanger. Starting by finding the fluid temperature profiles at a given timestep, the state equations for the plate can be solved forward with time.

When two internal flows are interacting with each other in the case of a transient counterflow heat exchanger, each flow must be related to the separating plate through an energy balance for each axial node to solve the problem – leading to a differential equation for the plate temperature that is integrated forward through time at each node in the axial direction. This is assumed to be a 1-D transient conduction problem and has been laid out with the following assumptions:

- the plate temperature in the x-direction has a constant temperature in the y-direction – or in other words, there is one node perpendicular to the flow direction and N nodes in the parallel,
- the fluid temperatures in the x-direction are changing but have constant temperatures in y-direction,
- the thermodynamic properties of the metal and each fluid remain constant through the heat exchanger,
- the left and right outside edges of the plate are assumed to be adiabatic – meaning that there is no heat transfer at these edges with the surroundings, and
- symmetry is used to assume an adiabatic boundary in the y-direction.

3.2.1 Hot Flow Energy Balances

Starting with the hot fluid, nodal energy balances are done as shown in **Figure 6.**

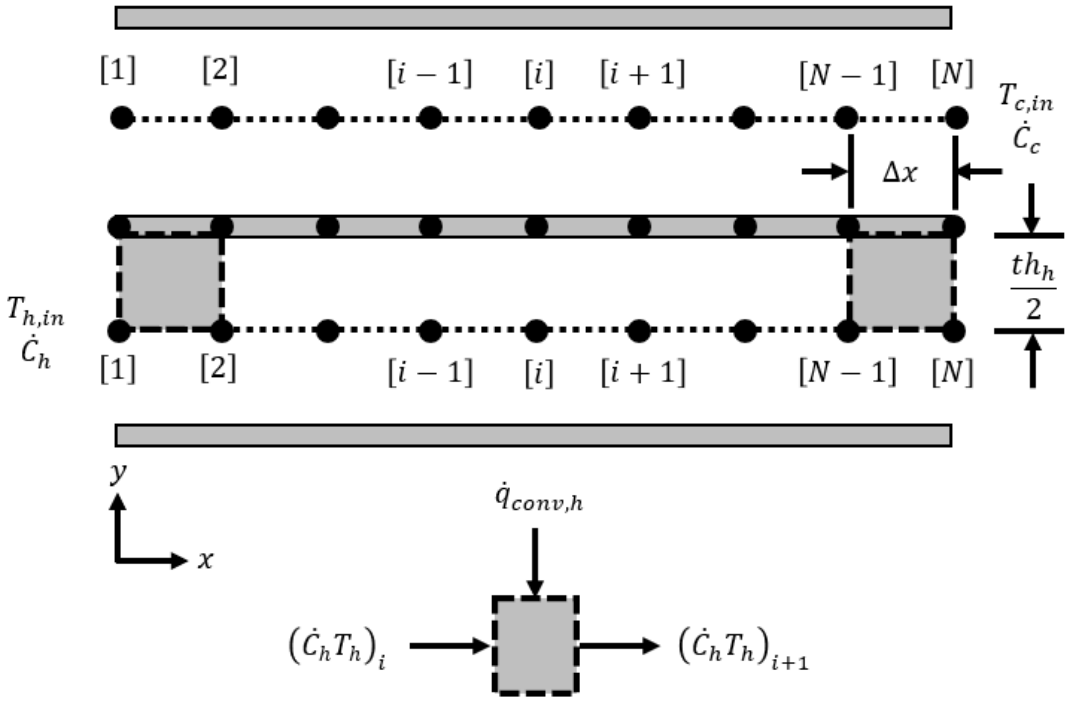

Figure 6. Energy balances on hot fluid.

For internal forced convection in the hot fluid, starting with the control volume between nodes one and two:

$$\left(\dot{C}_h T_h\right)_1 + \dot{q}_{conv,h} = \left(\dot{C}_h T_h\right)_2 \qquad (3.1)$$

The first term corresponds to the enthalpy crossing the boundary at node one, which is also the hot inlet; therefore, properties are known for this state. The second term corresponds to the convective heat transfer between the metal wall and the hot fluid. It is important to use an average temperature for this since the heat is technically being transferred at the temperature average between nodes one and two. Additionally, the total thermal conductance of each fluid

must be divided by the number of nodes, N. The third term corresponds to the enthalpy crossing the boundary at node two.

Next, the equation is further simplified and solved explicitly.

$$\left(\dot{C}_h T_h\right)_1 + \frac{UA_h}{N-1}\left(T_{m,avg} - T_{h,avg}\right) = \left(\dot{C}_h T_h\right)_2 \rightarrow$$

$$\left(\dot{C}_h T_h\right)_1 + \frac{UA_h}{N-1}\left[0.5\left(T_{m,1} + T_{m,2}\right) - 0.5\left(T_{h,1} + T_{h,2}\right)\right] = \left(\dot{C}_h T_h\right)_2 \rightarrow$$

$$\left(\dot{C}_h T_h\right)_1 + \frac{UA_h}{2(N-1)}\left[T_{m,1} + T_{m,2} - T_{h,1} - T_{h,2}\right] = \left(\dot{C}_h T_h\right)_2 \rightarrow$$

$$\left(\dot{C}_h T_h\right)_1 + \frac{UA_h}{2(N-1)}\left[T_{m,1} + T_{m,2} - T_{h,1}\right] = \left[\frac{UA_h}{2(N-1)} + \dot{C}_{h,2}\right] T_{h,2} \rightarrow$$

$$T_{h,2} = \frac{1}{\left(\frac{UA_h}{2(N-1)} + \dot{C}_{h,2}\right)}\left[\left(\dot{C}_h T_h\right)_1 + \frac{UA_h}{2(N-1)}\left[T_{m,1} + T_{m,2} - T_{h,1}\right]\right] \quad (3.2)$$

It is possible to solve for the hot fluid temperature at node two as shown above. To find the hot flow temperature at each node, a similar formula is used.

$$T_{h,i+1} = \frac{1}{\left(\frac{UA_h}{2(N-1)} + \dot{C}_{h,i+1}\right)}\left[\left(\dot{C}_h T_h\right)_i + \frac{UA_h}{2(N-1)}\left[T_{m,i} + T_{m,i+1} - T_{h,i}\right]\right] \quad (3.3)$$

After this has been entered with the prescribed inputs, the hot flow temperature at each node is known. This means that the hot flow temperature at node N is the hot flow outlet temperature.

3.2.2 Cold Flow Energy Balances

Proceeding to the cold fluid, nodal energy balances are done as shown in **Figure 7**.

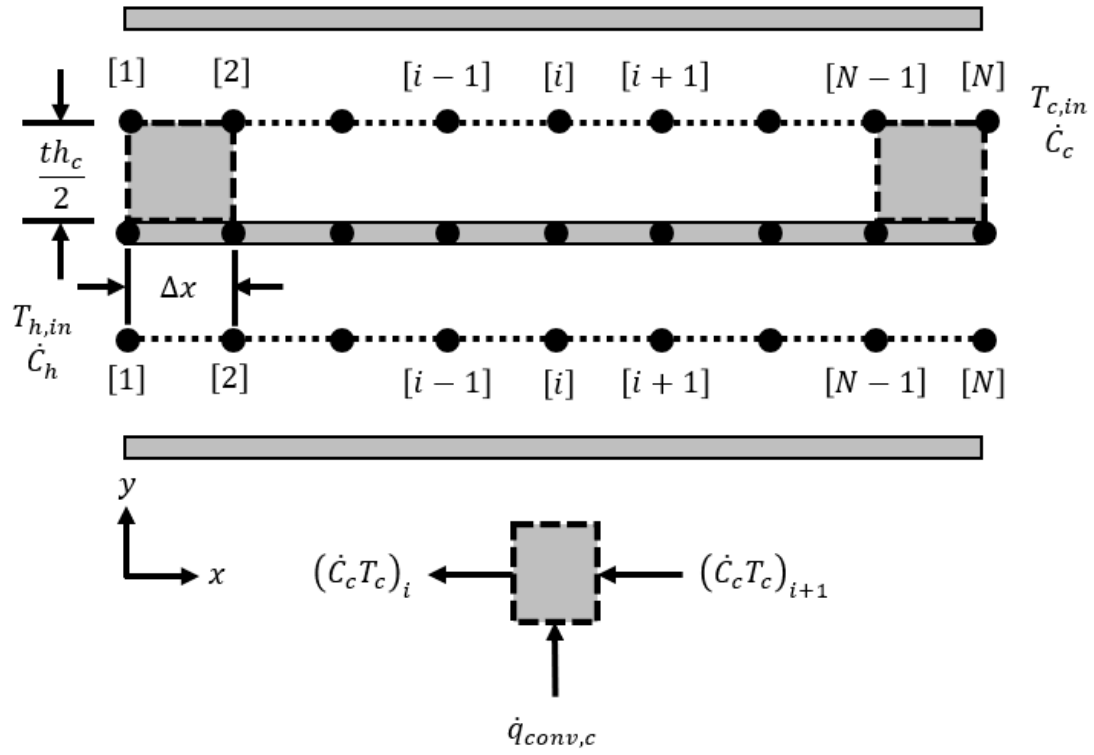

Figure 7. Energy balances on cold fluid.

For internal forced convection in the cold fluid, starting with the control volume between nodes N and $N-1$:

$$\left(\dot{C}_c T_c\right)_N + \dot{q}_{conv,c} = \left(\dot{C}_c T_c\right)_{N-1} \qquad (3.4)$$

The first term corresponds to the enthalpy crossing the boundary at node N, which is also the cold inlet; therefore, properties are known for this state. The second term corresponds to the convective heat transfer between the metal wall and the cold fluid. It is important to use an average temperature for this since the heat is technically being transferred at the temperature average between nodes N and $N-1$. Additionally, the total thermal conductance of each fluid must be divided by the number of nodes, N. The third term corresponds to the enthalpy crossing the boundary at node $N-1$.

Next, the equation is further simplified and solved explicitly.

$$\left(\dot{C}_c T_c\right)_N + \frac{UA_c}{(N-1)}\left(T_{m,avg} - T_{c,avg}\right) = \left(\dot{C}_c T_c\right)_{N-1} \rightarrow$$

$$\left(\dot{C}_c T_c\right)_N + \frac{UA_c}{(N-1)}\left[0.5\left(T_{m,N} + T_{m,N-1}\right) - 0.5\left(T_{c,N} + T_{c,N-1}\right)\right] = \left(\dot{C}_c T_c\right)_{N-1} \rightarrow$$

$$\left(\dot{C}_c T_c\right)_N + \frac{UA_c}{2(N-1)}\left[T_{m,N} + T_{m,N-1} - T_{c,N} - T_{c,N-1}\right] = \left(\dot{C}_c T_c\right)_{N-1} \rightarrow$$

$$\left(\dot{C}_c T_c\right)_N + \frac{UA_c}{2(N-1)}\left[T_{m,N} + T_{m,N-1} - T_{c,N}\right] = \left[\frac{UA_c}{2(N-1)} + \dot{C}_{c,N-1}\right] T_{c,N-1} \rightarrow$$

$$T_{c,N-1} = \frac{1}{\left(\frac{UA_c}{2(N-1)} + \dot{C}_{c,N-1}\right)}\left[\left(\dot{C}_c T_c\right)_N + \frac{UA_c}{2(N-1)}\left[T_{m,N} + T_{m,N-1} - T_{c,N}\right]\right] \qquad (3.5)$$

It is possible to solve for the cold fluid temperature at node $N-1$ as shown above. To find the cold flow temperature at each node, a similar formula is used.

$$T_{c,i-1} = \frac{1}{\left(\frac{UA_c}{2(N-1)} + \dot{C}_{c,i-1}\right)}\left[\left(\dot{C}_c T_c\right)_i + \frac{UA_c}{2(N-1)}\left[T_{m,i} + T_{m,i-1} - T_{c,i}\right]\right] \qquad (3.6)$$

After this has been entered with the prescribed inputs, the cold flow temperature at each node is known. This means that the cold flow temperature at node 1 is the cold flow outlet temperature.

3.2.3 Metal Energy Balances

Proceeding with the metal nodes, nodal energy balances are done as shown in **Figure 8**.

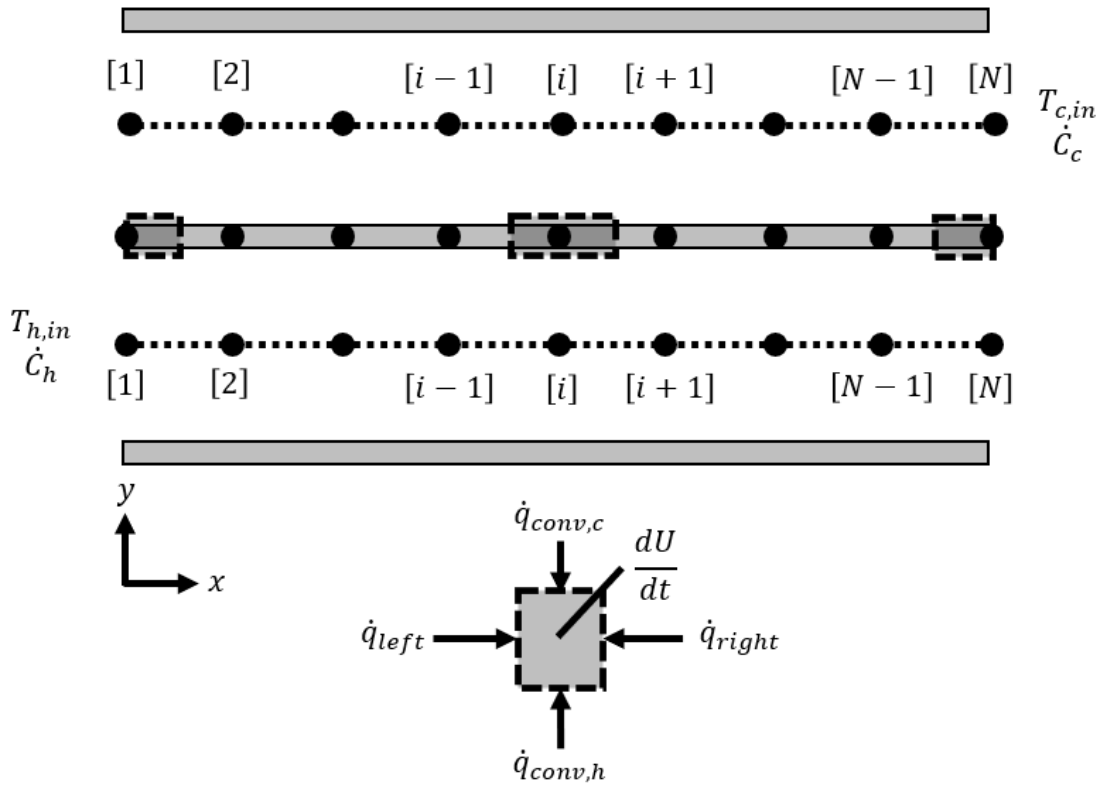

Figure 8. Energy balances on metal nodes.

The fundamental energy balance for the control volume is:

$$\frac{dU}{dt} = \dot{q}_{left} + \dot{q}_{right} + \dot{q}_{conv,h} + \dot{q}_{conv,c} \qquad (3.7)$$

On the right side of the equation, the first term corresponds to the conduction through the metal from the left. The second term corresponds to the conduction through the metal from the right. The third term corresponds to the convective heat transfer between the wall and the hot fluid. The fourth term corresponds to the convective heat transfer between the wall and the cold fluid. The total thermal conductance of each fluid must be divided by the number of nodes, N. A single temperature value for each metal node is assumed.

For nodes two through $N - 1$, the equation can be simplified to:

$$\left(\frac{C_{tot}}{N-1}\right)\frac{dT_{m,i}}{dt} = \frac{\left(T_{m,i-1} - T_{m,i}\right)}{R_{cond}} + \frac{\left(T_{m,i+1} - T_{m,i}\right)}{R_{cond}} + \frac{UA_h}{N-1}\left(T_{h,i} - T_{m,i}\right) + \frac{UA_c}{N-1}\left(T_{c,i} - T_{m,i}\right) \rightarrow$$

$$\frac{dT_{m,i}}{dt} = \frac{N-1}{R_{cond}C_{tot}}\left(T_{m,i-1} + T_{m,i+1} - 2T_{m,i}\right) + \frac{UA_h}{C_{tot}}\left(T_{h,i} - T_{m,i}\right) + \frac{UA_c}{C_{tot}}\left(T_{c,i} - T_{m,i}\right) \quad (3.8)$$

For node one, a similar equation can be used; however, conduction from the left will be neglected since the left metal surface at node one is assumed to be an adiabatic surface. This means there is no heat transfer from the left. The control volume and overall conductance must also be divided by two since heat is being transferred over a control volume half the size of the internal nodes.

$$\frac{dT_{m,1}}{dt} = \frac{2(N-1)}{R_{cond}C_{tot}}\left(T_{m,2} - T_{m,1}\right) + \frac{UA_h}{C_{tot}}\left(T_{h,1} - T_{m,1}\right) + \frac{UA_c}{C_{tot}}\left(T_{c,1} - T_{m,1}\right) \quad (3.9)$$

For node N, a similar equation can be used; however, conduction from the right will be neglected since the right metal surface at node N is assumed to be an adiabatic surface. The control volume and overall conductance must also be divided by two since heat is being transferred over a control volume half the size of the internal nodes.

$$\frac{dT_{m,N}}{dt} = \frac{2(N-1)}{R_{cond}C_{tot}}\left(T_{m,N-1} - T_{m,N}\right) + \frac{UA_h}{C_{tot}}\left(T_{h,N} - T_{m,N}\right) + \frac{UA_c}{C_{tot}}\left(T_{c,N} - T_{m,N}\right) \quad (3.10)$$

Now, it is possible to solve for the change in temperature with respect to time for each of the metal nodes and therefore, the metal node temperatures are determined at each timestep. Equations (3.8), (3.9), and (3.10) are the state equations that must be integrated. The model is implemented using MATLAB's built-in ODE45 solver – which evaluates the state equation by integrating through time for each node in the axial direction. The simulation time, t_{sim}, is divided equally into M timesteps.

3.3 Model Specification

To demonstrate model functionality, key graphs are compared for varied inputs and simulation conditions for the solution are presented.

3.3.1 Simulation Conditions

The inputs in **Table 2** are specified for the first set of graphs in the model demonstration section. These values are primarily compiled from various sources documenting start-up conditions at the recuperators for some examples of sCO2 Brayton cycles. Some were solved for using an implicit solver that used an arbitrary mass flow rate, and the values should not be considered to be highly accurate for a standard cycle.

Table 2. Simulation Conditions for Constant Inputs

Property	Value	Units	Property	Value	Units
UA_h	40	[W/K]	$T_{m,ini}$	300	[K]
UA_c	40	[W/K]	$T_{h,in}$	875	[K]
C_{tot}	80	[J/K]	$T_{c,in}$	375	[K]
$R_{cond,tot}$	0.01, 1, 1e6	[K/W]	$\dot{C}_{h,in}$	20	[W/K]
τ	C_{tot}/UA	[s]	$\dot{C}_{c,in}$	40	[W/K]
t_{sim}	5τ	[s]	N	101	[-]
t_{span}	$0 \ldots t_{sim}$	[s]	M	121	[-]

These parameters are constants and do not change throughout simulation – meaning there is no ramping in the fluid inlet parameters. Later graphs will look at what happens when linear ramping parameters are specified for the fluid inlet temperatures and capacitance rates.

3.3.2 Model Demonstration

The graphs in **Figure 9, 10, 11** compare the effects of axial conduction by changing the total axial conduction resistance in the metal. This model will include axial conduction to add more precision to the resulting graphs. Axial conduction is effectively ignored at high values of $R_{cond,tot}$ since the term in the energy balance would approach zero. The non-dimensionalized x-axis position parameter is $x^* = x/L$.

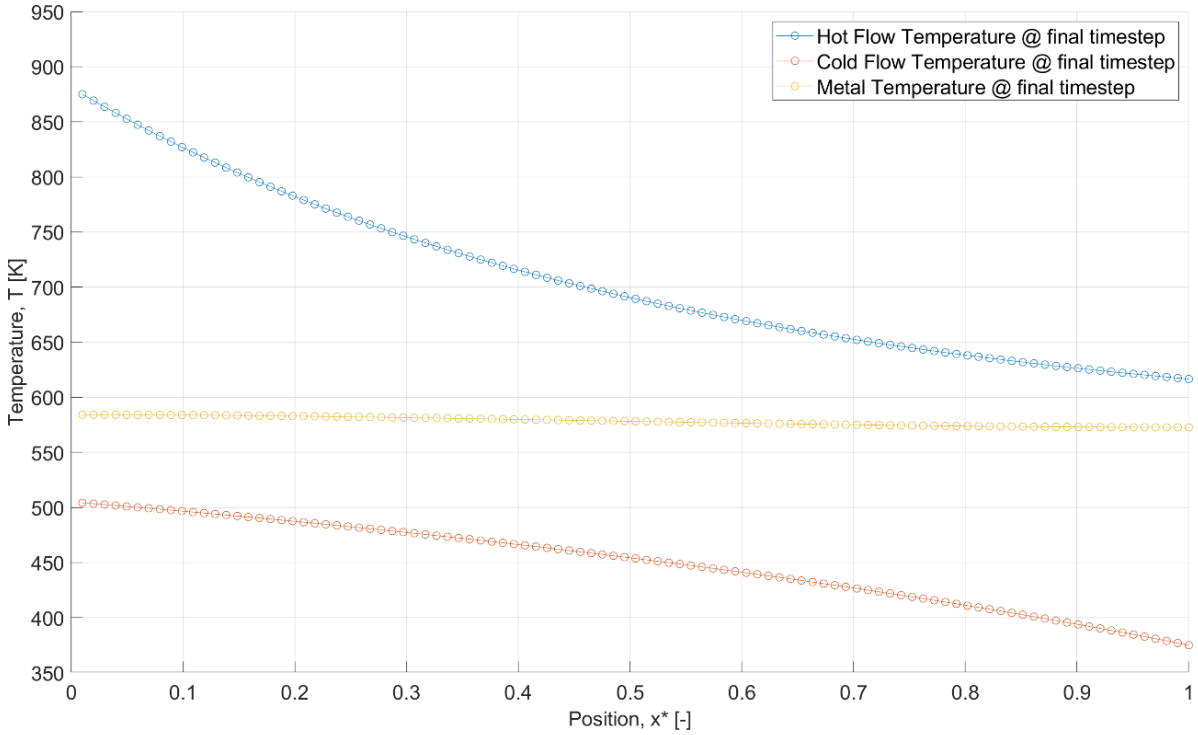

Figure 9. Temperature profiles for hot flow, cold flow, and metal at $R_{cond,tot} = 0.01\ [K/W]$.

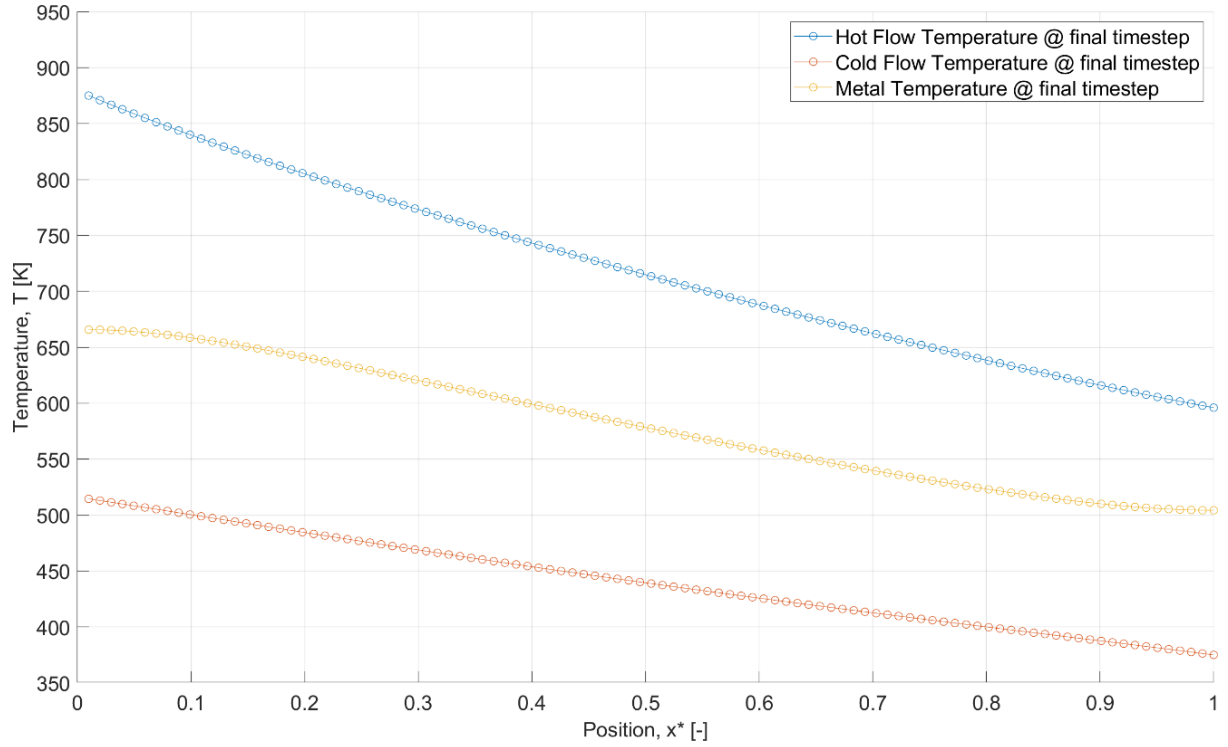

Figure 10. Temperature profiles for hot flow, cold flow, and metal at $R_{cond,tot} = 1\ [K/W]$.

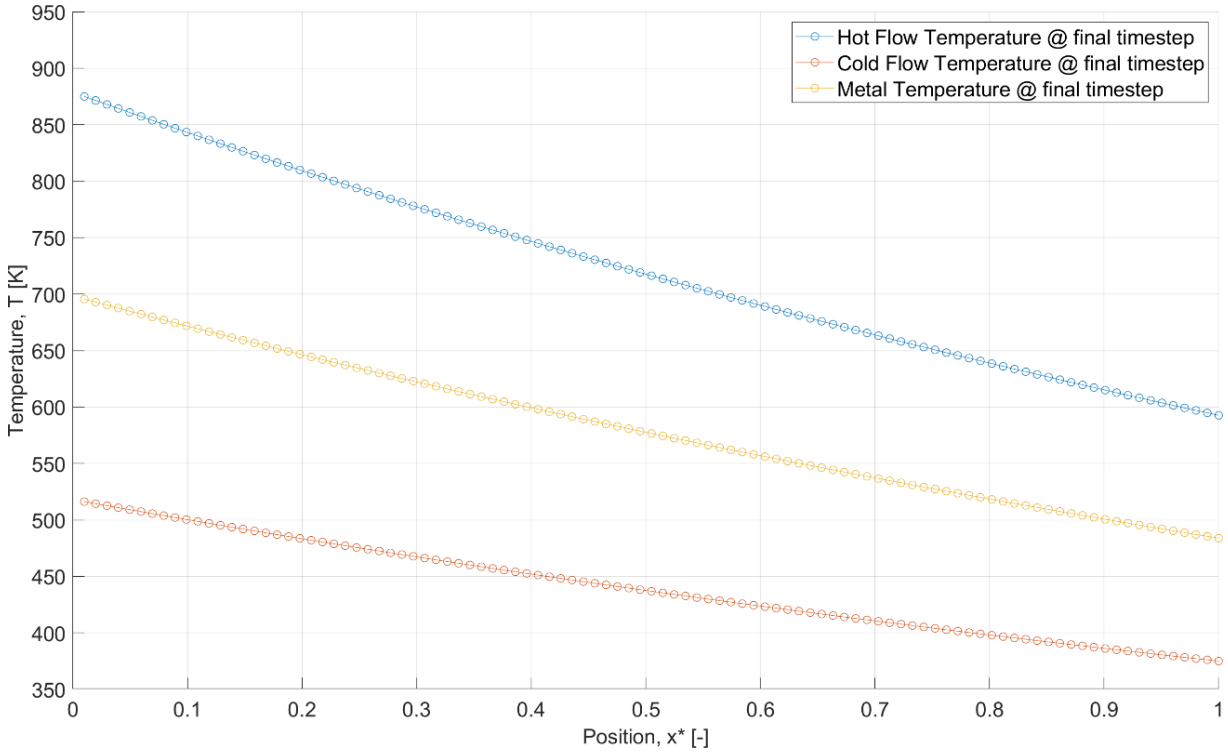

Figure 11. Temperature profiles for hot flow, cold flow, and metal at $R_{cond,tot} = 1e6\ [K/W]$.

Next, the temperature profile of the metal is examined at various timesteps throughout simulation in the graphs in **Figure 12, 13, 14**. The total simulation time is 12 seconds, so this has been split into 5 equal segments of time – which makes each line of the graph separated by 2.4 seconds. The initial temperature of the metal nodes is constant at each nodal position then increases as heat is transferred from the hot fluid to the metal to the cold fluid. The effects of changing the total axial resistance to conduction in the metal is demonstrated in the following three graphs. Axial conduction is effectively ignored at high values of $R_{cond,tot}$ since the term in the energy balance would approach zero.

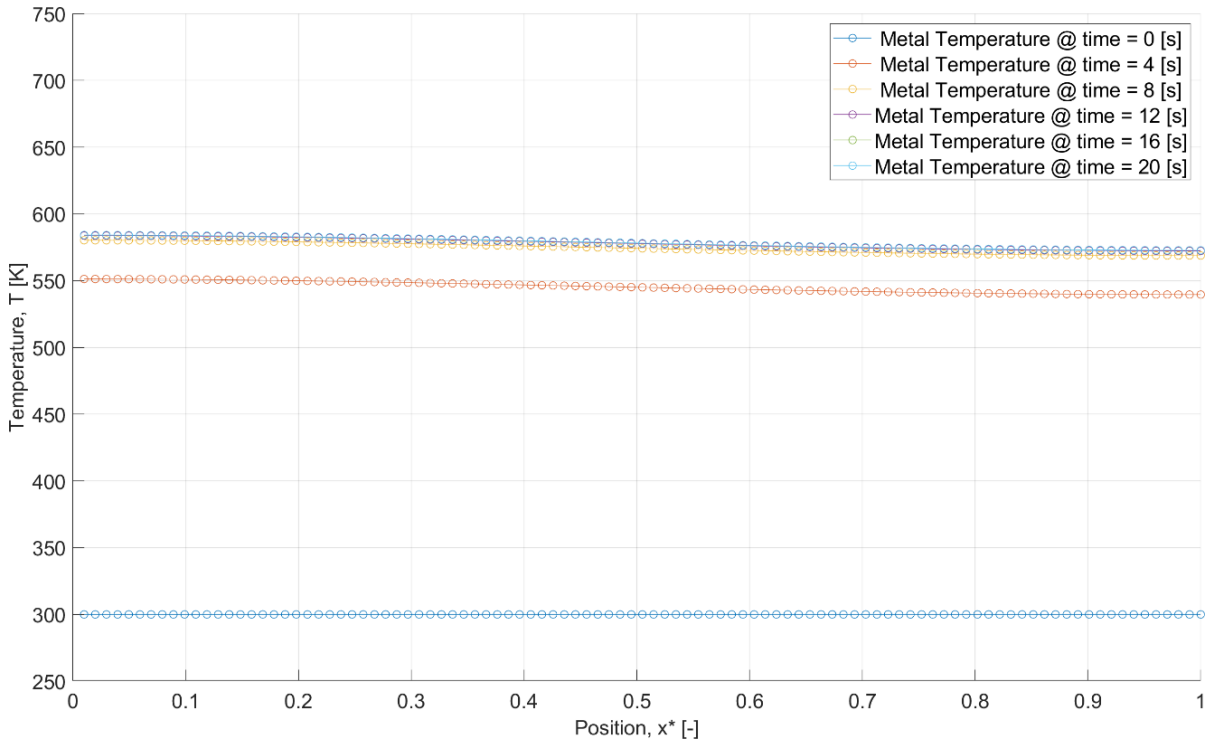

Figure 12. Metal temperature profiles at $R_{cond,tot} = 0.01\ [K/W]$.

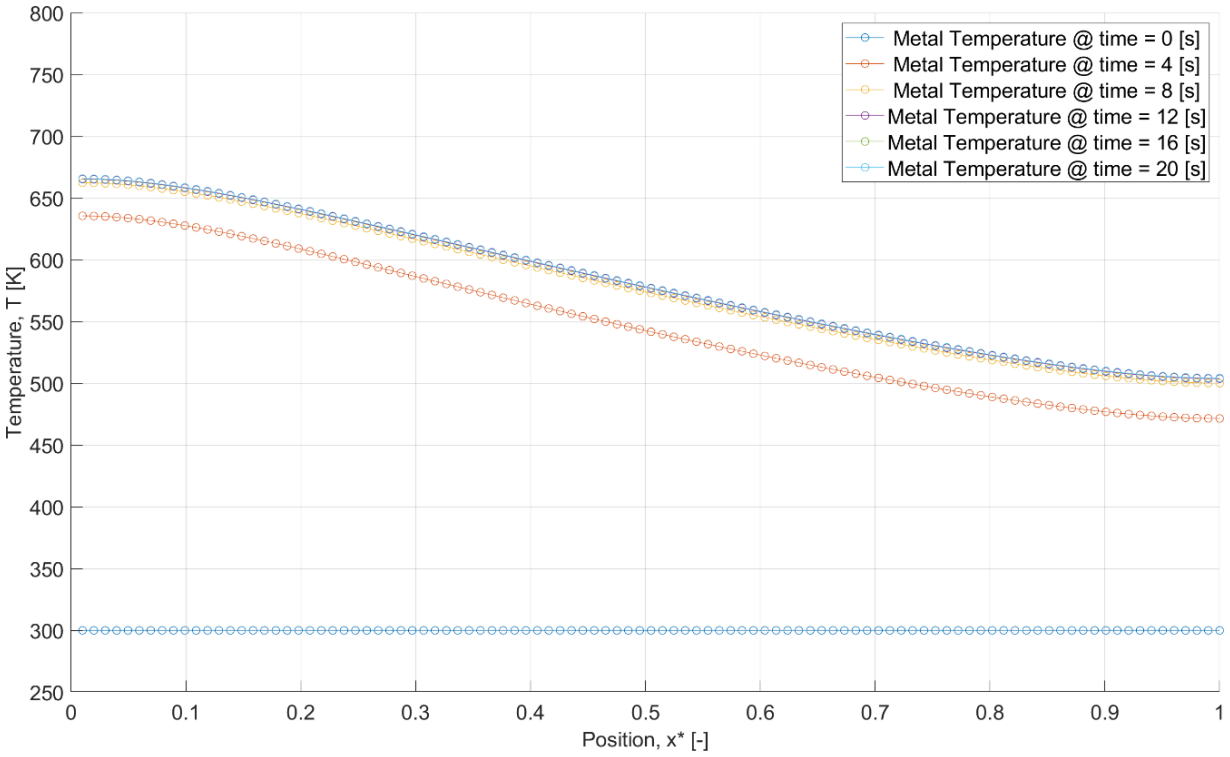

Figure 13. Metal temperature profiles at $R_{cond,tot} = 1\ [K/W]$.

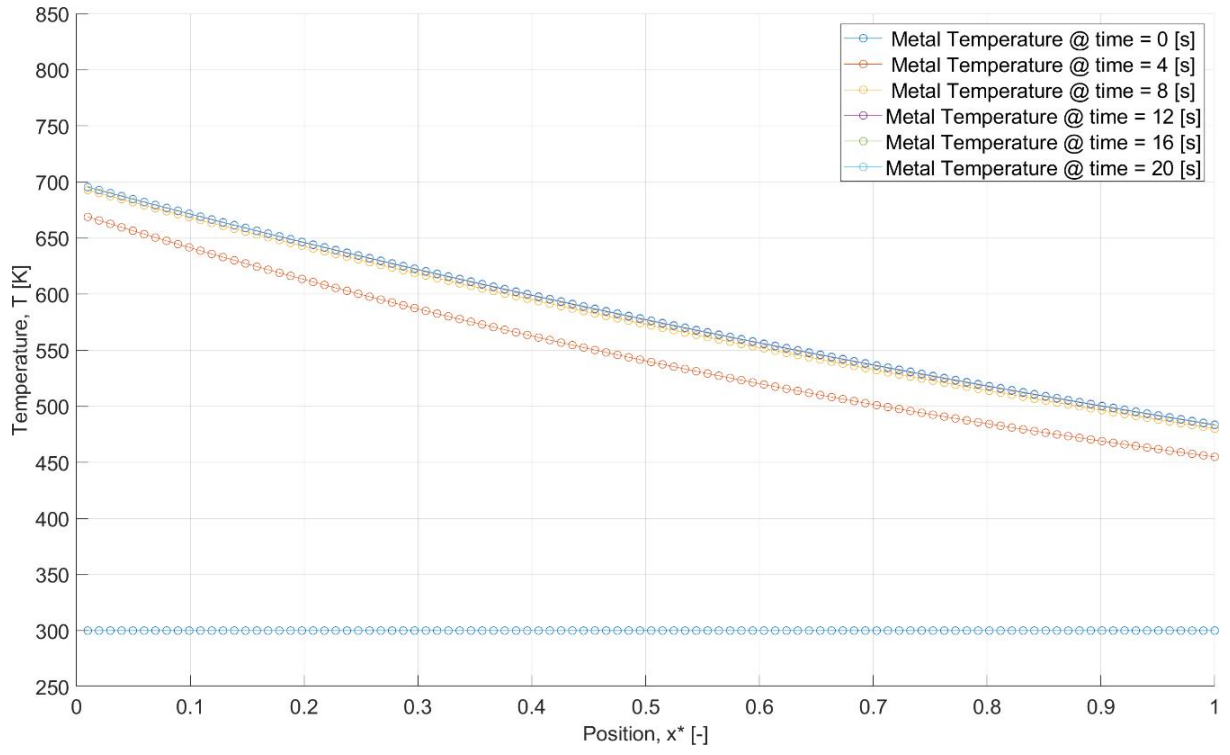

Figure 14. Metal temperature profiles at $R_{cond,tot} = 1e6\ [K/W]$.

The graphs in **Figure 15, 16, 17** compare the metal temperature time response. The graphs show that the metal temperatures reach an elevated steady-state temperature when axial conduction is neglected. The entire temperature profile of the metal is more uniform at lower values of $R_{cond,tot}$ – proving that the inclusion of a massive axial conduction term in the metal has significant impacts on the temperature response of the heat exchanger.

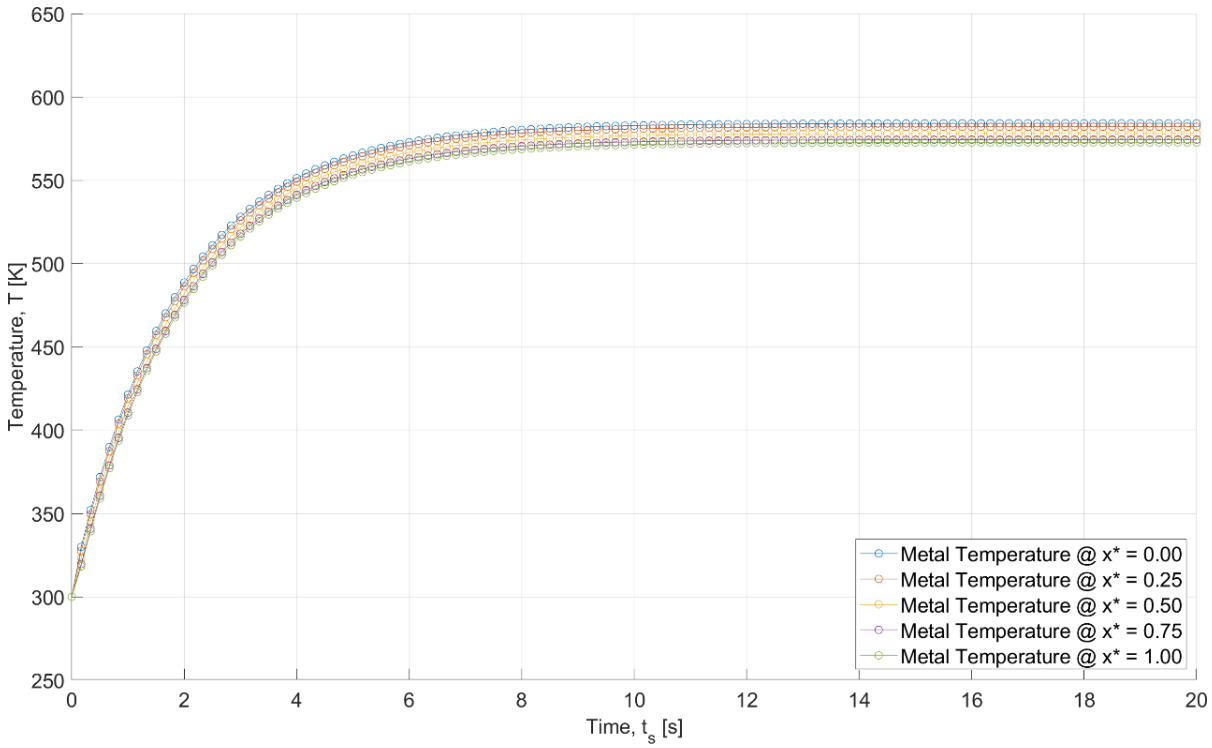

Figure 15. Metal temperature time response at $R_{cond,tot} = 0.01\ [K/W]$.

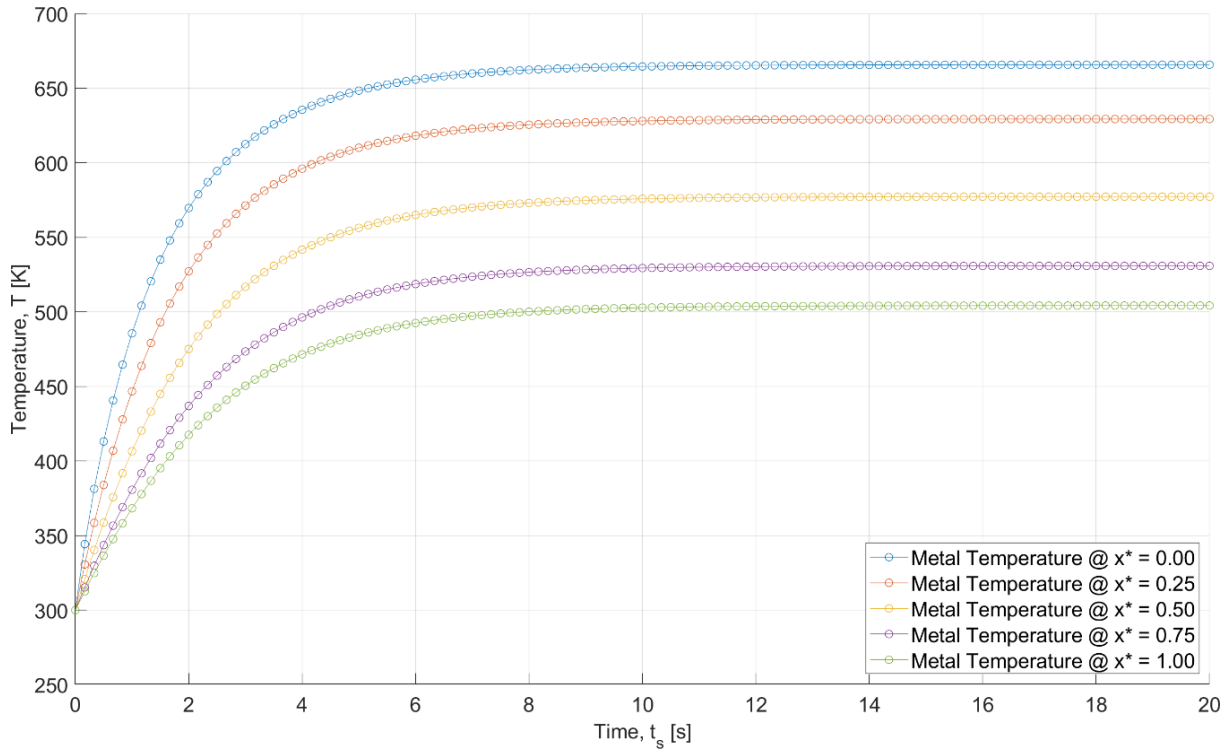

Figure 16. Metal temperature time response at $R_{cond,tot} = 1\ [K/W]$.

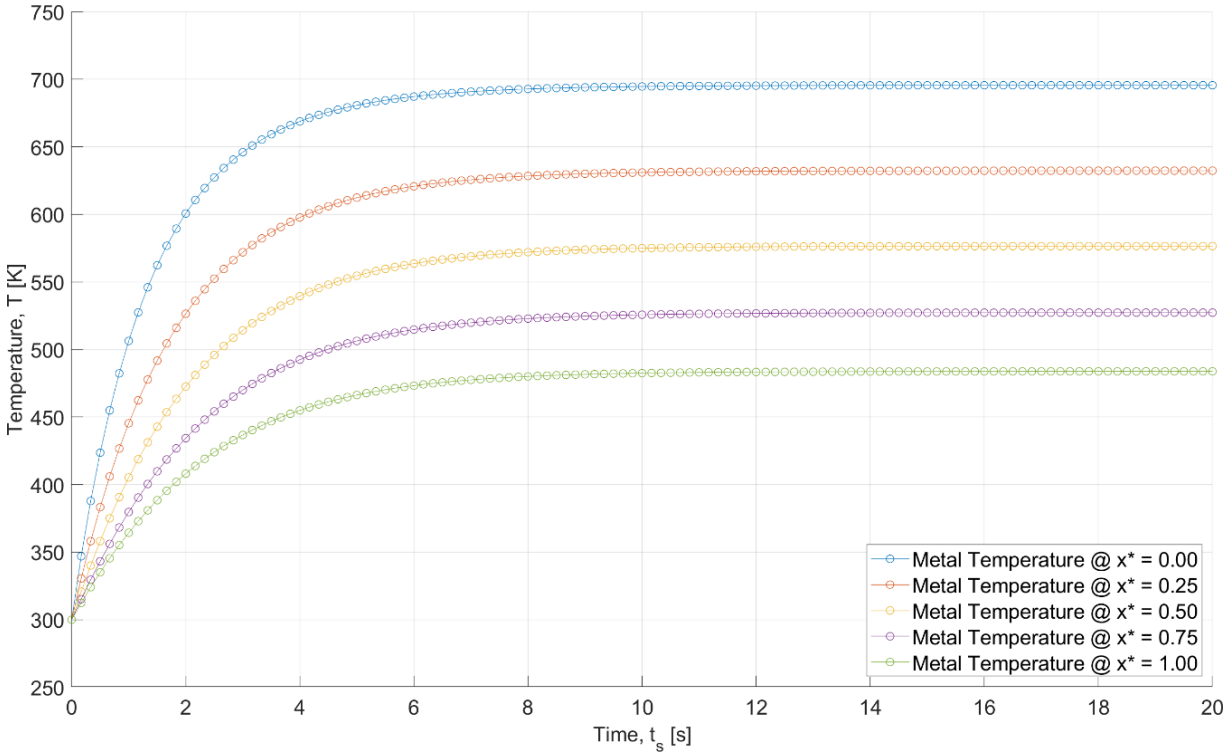

Figure 17. Metal temperature time response at $R_{cond,tot} = 1e6\ [K/W]$.

3.4 Model Verification

The results of this transient heat exchanger numerical model can be compared to results from multiple types of sources including those from analytical solutions.

3.4.1 Steady-State Analytical Solution (Effectiveness-NTU Model)

The following graphs in **Figure 18, 19, 20** show a comparison of the numerical transient solution, when axial conduction resistance in the metal is neglected, after clearly reaching steady-state versus the effectiveness-NTU solution. In addition to comparing one against the other, a nodal study has also been done to determine the changes in percent difference. The goal in doing this study is to minimize changes in percent difference while investigating the relationship between temperature profiles at the inlet and outlet versus heat exchanger sizing. The graph in **Figure 18** shows a clear agreement between the transient model at steady-state and the effectiveness-NTU solution.

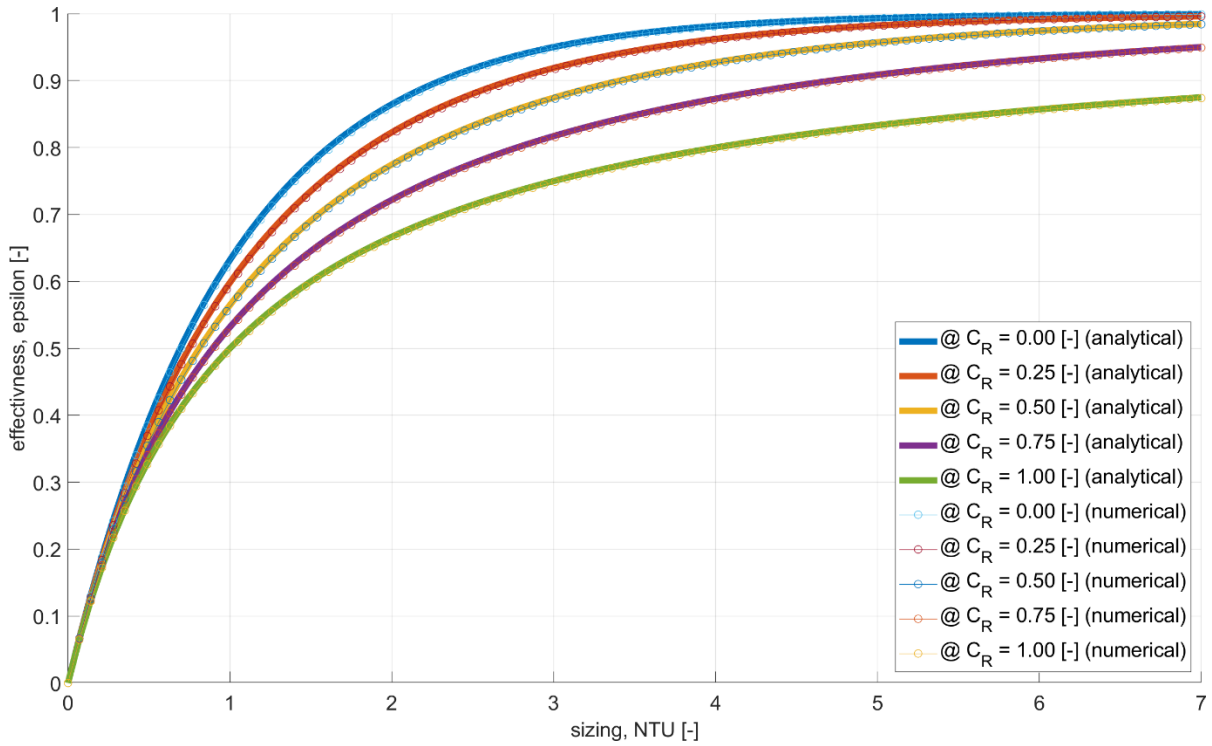

Figure 18. Comparison to eff-NTU solution for varied capacitance ratios at $N = 101$.

The graphs in **Figure 19** and **Figure 20** show an increased difference in temperatures as the number of nodes decreases; therefore, it is important to use a high number of nodes to maximize model accuracy. The suggested number of nodes is 101 since this keeps the percent difference under 1% for all values of NTU.

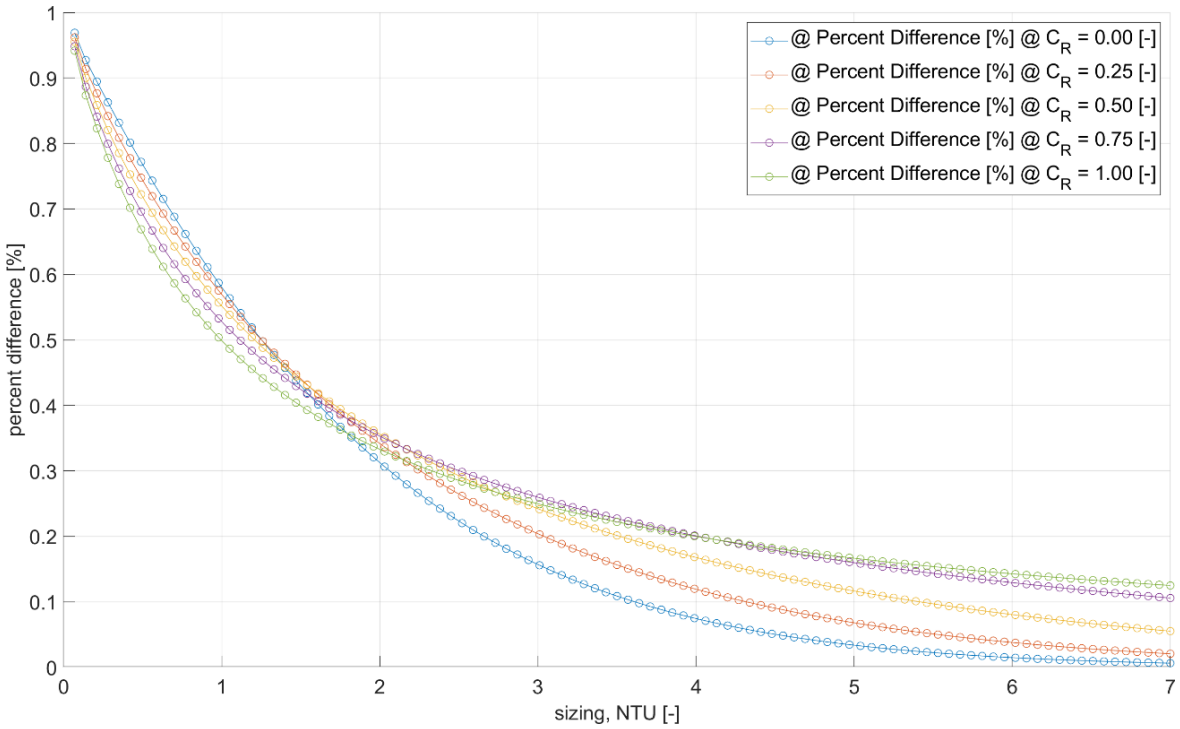

Figure 19. Percent difference in effectiveness for both solutions when $N = 101$.

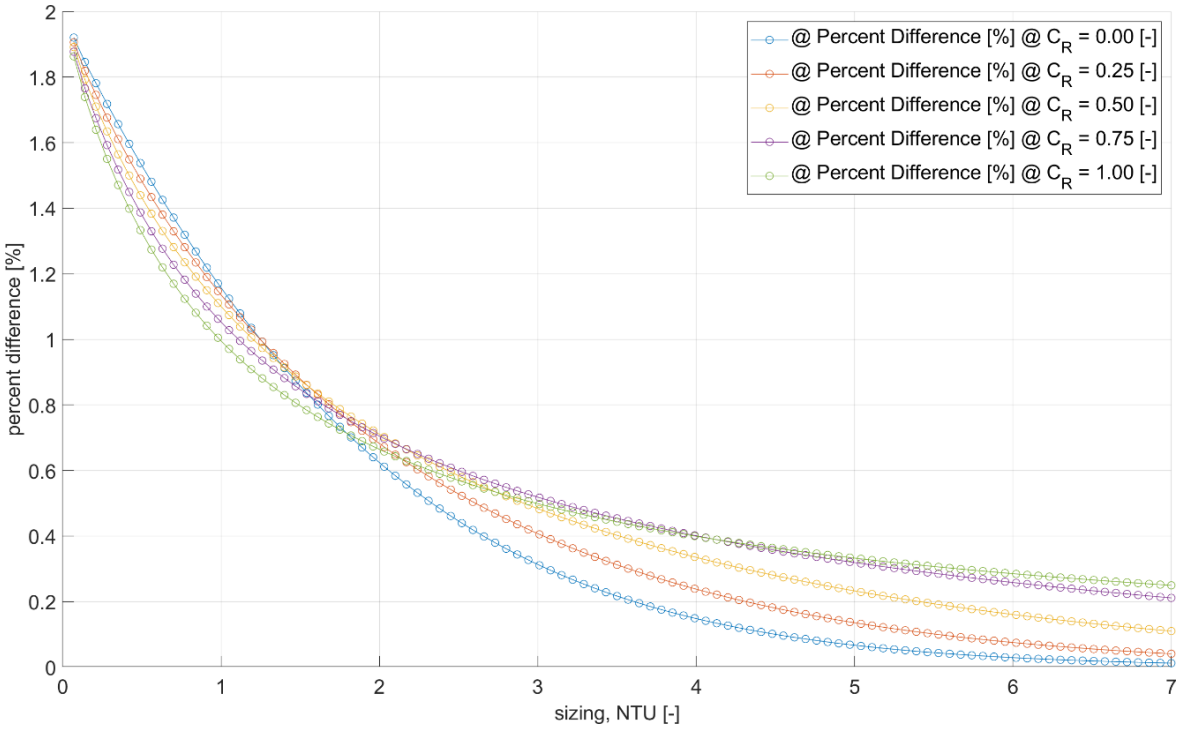

Figure 20. Percent difference in effectiveness for both solutions when $N = 51$.

Further analysis was done when $NTU = 1$ to examine the number of nodes needed for accuracy at a constant value of NTU. As shown by **Figure 21, 22** the percent difference is close to 1% when $N = 101$.

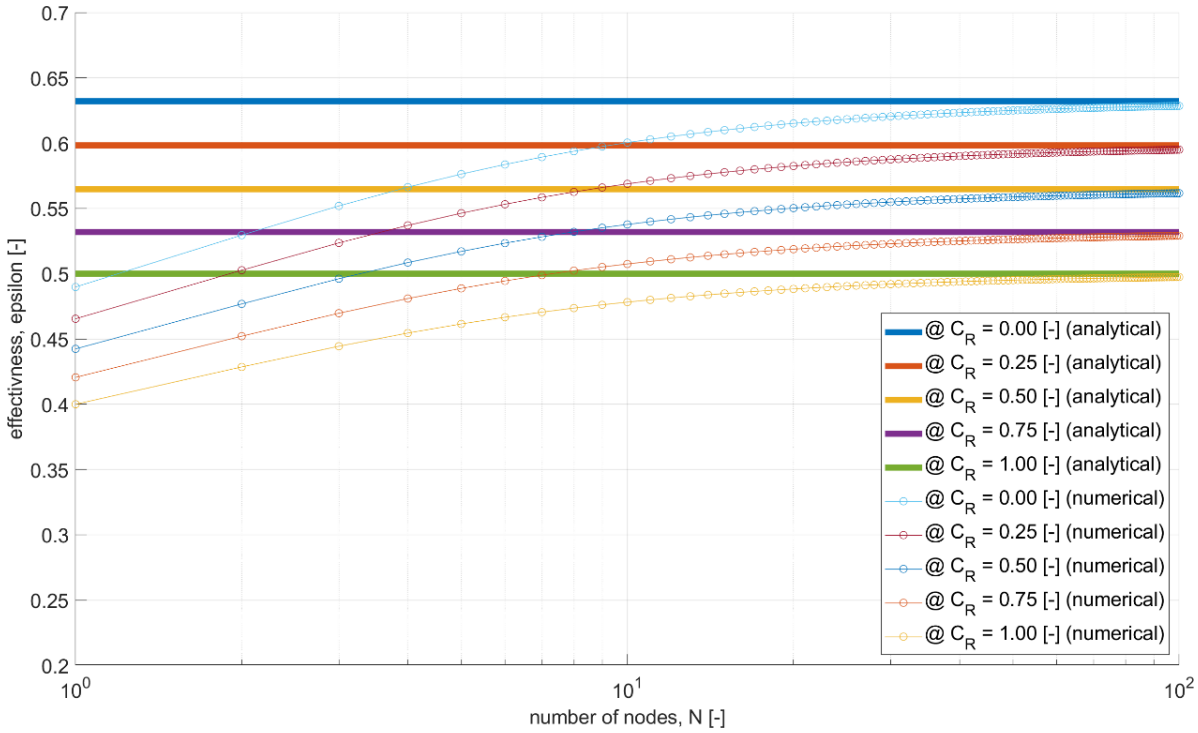

Figure 21. Comparison to eff-NTU solution for varied capacitance ratios for $NTU = 1$.

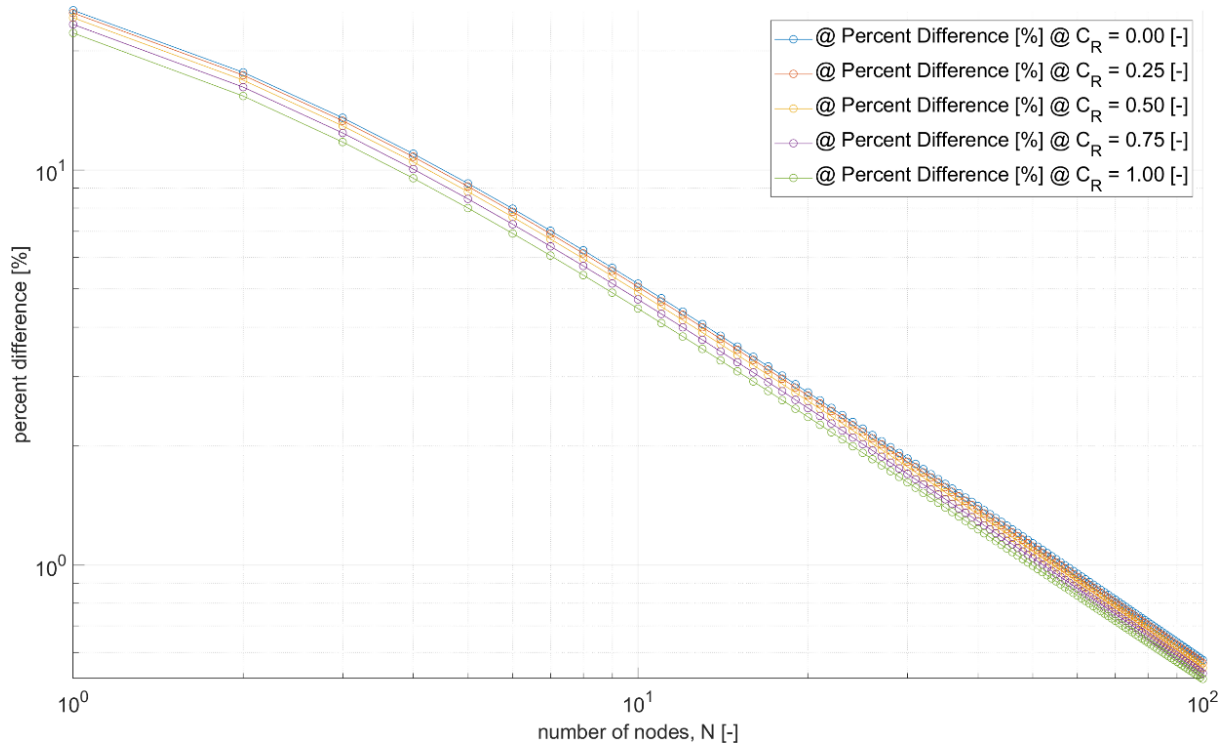

Figure 22. Percent difference in effectiveness for both solutions when $NTU = 1$.

3.4.2 Transient Analytical Solution

The first comparison looks at the following graph in **Figure 23** for the intercooler and precooler solutions for the case where $\bar{C}_w^* > 5$, $\dot{C}_{min}/\dot{C}_{max} = 0$, and $R^* = 1$. This model uses $\bar{C}_w^* = 1e6\ [-]$ to solve.

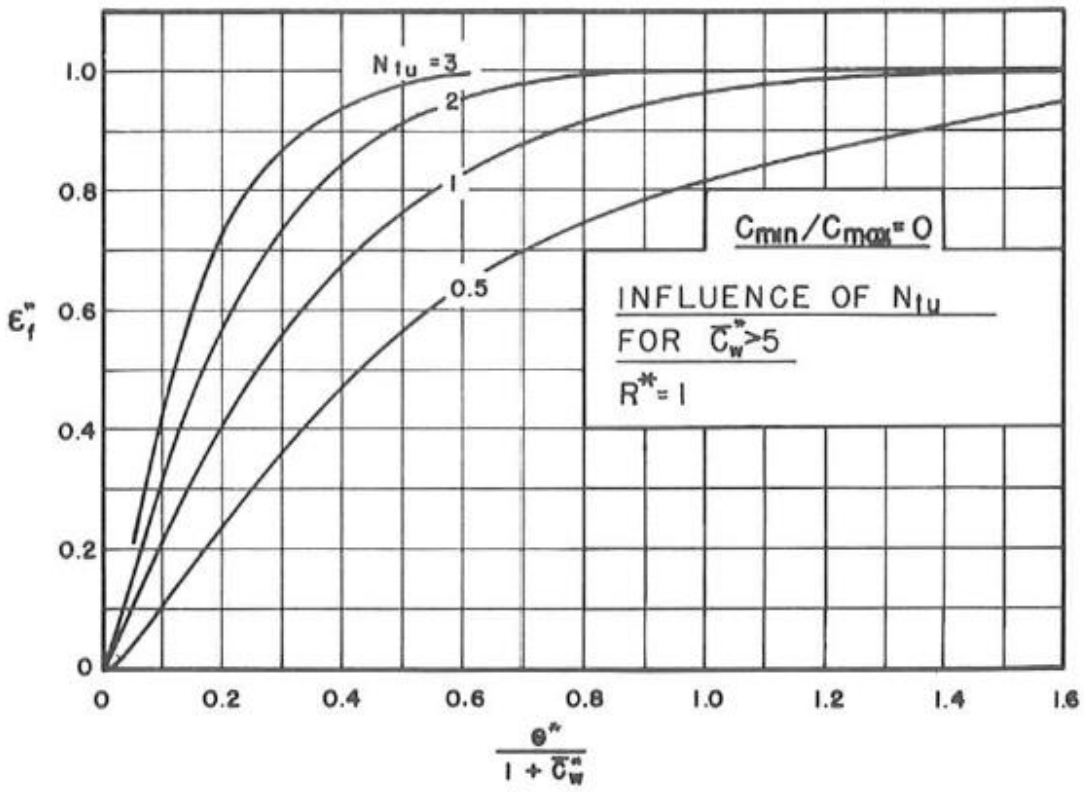

Figure 23. Intercooler and precooler solutions for problems with $\bar{C}_w^* > 5$ [2].

Figure 23 presents the electromechanical analog results analyzing the influence of heat exchanger sizing, wall-to-fluid capacity ratio, and dimensionless time, on the normalized effectiveness parameter. As shown below, the numerical model presents similar results to that of the preceding transient model. The y-axis parameter is a generalized dimensionless parameter that normalizes changes in the time-dependent effectiveness for each fluid. This data has been digitized from [2], but practically, this means that the y-axis parameter is the ratio of the fluid effectiveness at any time to the fluid effectiveness at steady-state, and it can be expressed as

$$\varepsilon_f^* = \frac{\varepsilon_f}{\varepsilon_{fss}} \qquad (3.11)$$

The transient fluid effectiveness,

$$\varepsilon_f = \frac{\dot{q}_c}{\dot{q}_{max}} \rightarrow \varepsilon_f = \frac{\dot{C}_c\left(T_{c,out} - T_{c,in}\right)}{\dot{C}_{min}\left(T_{h,in} - T_{c,in}\right)} \quad (3.12)$$

For $R^* = 1$, the steady-state fluid effectiveness,

$$\varepsilon_{fss} = \frac{NTU}{1 + NTU} \quad (3.13)$$

The primary transient model comparison comes from [2]. This study models the counterflow heat exchanger using these three coupled, linear, partial differential equations:

$$\left\{\frac{T_h - T_w}{R_h L}\right\} = -\left\{\frac{\bar{C}_h}{L}\frac{\partial T_h}{\partial \theta}\right\} + \left\{C_h \frac{\partial T_h}{\partial x}\right\} \quad (3.14)$$

$$\left\{\frac{T_w - T_c}{R_c L}\right\} = \left\{\frac{\bar{C}_c}{L}\frac{\partial T_c}{\partial \theta}\right\} + \left\{C_c \frac{\partial T_c}{\partial x}\right\} \quad (3.15)$$

$$\left\{\frac{T_h - T_w}{R_h}\right\} - \left\{\frac{T_w - T_c}{R_c}\right\} = \left\{\bar{C}_w \frac{\partial T_w}{\partial \theta}\right\} \quad (3.16)$$

These equations mimic the energy balances as previously discussed with one discrepancy – the model in this thesis does not include a $\bar{C}_h$ or $\bar{C}_c$ value which corresponds to the heat capacity of the hot and cold fluid, respectively. Therefore, this model will be verified against situations in this model where these values are equal to zero. There are several non-dimensional parameters that have been defined in [2], and the most important ones are:

$$\theta^* = \frac{\theta}{\theta_{dmin}} \quad (3.17)$$

$$\theta_d^* = \frac{\theta_{dmin}}{\theta_{dmax}} \quad (3.18)$$

$$R^* = \frac{R_{min}}{R_{max}} \quad (3.19)$$

$$\bar{C}_w^* = \frac{\bar{C}_w}{\bar{C}_{min}} \quad (3.20)$$

$$C_R = \frac{C_{min}}{C_{max}} \quad (3.21)$$

θ is used here to represent time. θ_d^* and R^* may be equal to, greater than, or less than unity – the minimum subscript corresponds to the minimum of the fluid capacitance rates, C_c and C_h [2]. Because the model developed here does not include a $\bar{C}_h$ or $\bar{C}_c$ value, the value of $\bar{C}_{min}$ must be equal to zero; therefore, the wall-to-fluid capacity ratio, $\bar{C}_w^*$ is a large number approaching infinity in this model. By simplifying the equations for the non-dimensional parameters, a more obvious relationship between $\bar{C}_w^*$ and θ^* can be derived. The following steps show the derivation.

$$\theta_{dmin} = \frac{\bar{C}_{min}}{\dot{C}_{min}} \quad (3.22)$$

By rearranging equation (3.22),

$$\bar{C}_{min} = \theta_{dmin}\dot{C}_{min} \quad (3.23)$$

Then, substituting equation (3.23) into equation (3.20),

$$\bar{C}_w^* = \frac{\bar{C}_w}{\bar{C}_{min}} \rightarrow \bar{C}_w^* = \frac{\bar{C}_w}{\theta_{dmin}\dot{C}_{min}} \quad (3.24)$$

By rearranging equation (3.18),

$$\theta_{dmin} = \frac{\theta}{\theta^*} \quad (3.25)$$

Then, substituting equation (3.25) into equation (3.24),

$$\bar{C}_w^* = \frac{\bar{C}_w}{\theta_{dmin}\dot{C}_{min}} \rightarrow \bar{C}_w^* = \frac{\bar{C}_w}{\dot{C}_{min}}\frac{\theta^*}{\theta} \quad (3.26)$$

By rearranging equation (3.26),

$$\theta^* = \frac{\bar{C}_w^*\dot{C}_{min}\theta}{\bar{C}_w} \quad (3.27)$$

where $\bar{C}_w$ corresponds to the total heat capacity of the metal, C_{tot} from this model, the minimum fluid capacitance rate, $\dot{C}_{min}$ and θ is the time parameter in seconds. The x-axis parameter in **Figure 23** is expressed in terms of θ^* and $\bar{C}_w^*$ to best understand the impact of the wall-to-fluid capacity ratio on the model.

$$x = \frac{\theta^*}{1 + \bar{C}_w^*} \quad (3.28)$$

By substituting equation (3.27) into equation (3.28),

$$x = \frac{\bar{C}_w^*\dot{C}_{min}\theta}{\bar{C}_w(1 + \bar{C}_w^*)} \quad (3.29)$$

Equation (3.29) shows how the x-axis parameter begins to approach a finite value as $\bar{C}_w^*$ approaches infinity. For $\dot{C}_{min} = 20\ [W/K]$ and $\bar{C}_w = C_{tot} = 80\ [W/K]$, **Table 3** shows how the x-axis parameter changes as $\bar{C}_w^*$ approaches infinity.

Table 3. Derivation of x-axis Parameter Results

	θ [s]				
$\bar{C}_w^*$ [-]	0	0.5	1	2	5
5	0.000	0.104	0.208	0.417	1.042
20	0.000	0.119	0.238	0.476	1.190
1.00E+06	0.000	0.125	0.250	0.500	1.250
1.00E+15	0.000	0.125	0.250	0.500	1.250

As shown, the x-axis parameter approaches a finite value as $\bar{C}_w^*$ approaches infinity; therefore, the analysis that is done for various values of $\bar{C}_w^*$ [2] is valid for this model described in this paper. However, for small values of $\bar{C}_w^*$, it is important to consider how much error may be present. In most cases, large values have been used to negate error down to several decimal places. The maximum percent difference of roughly 2.5% can be found at approximately $x = 0.7143\ [-]$.

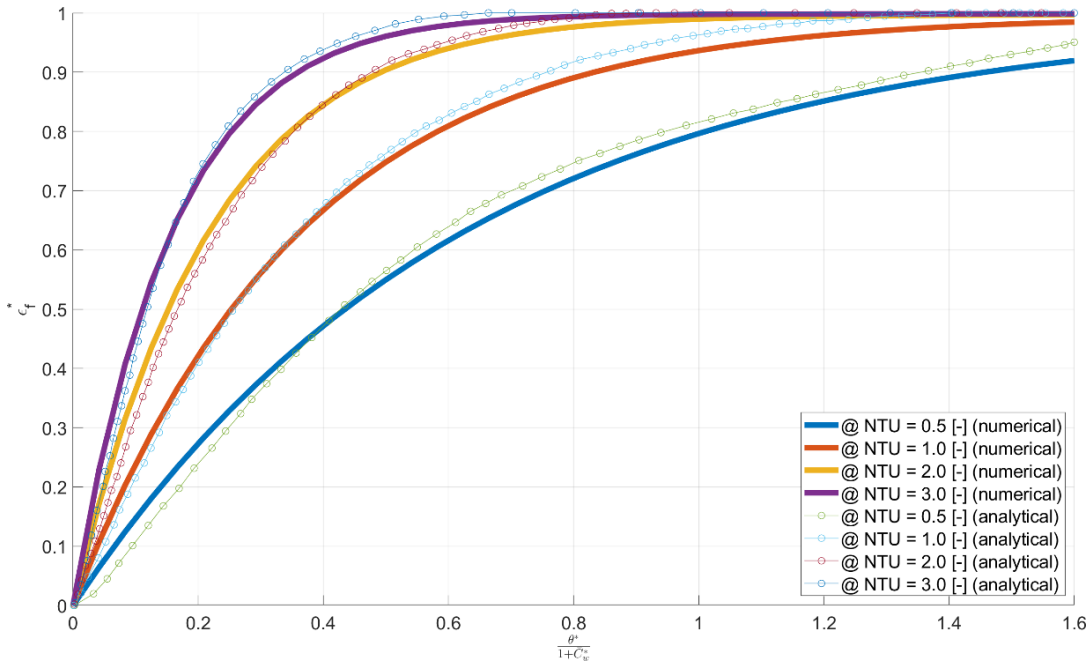

Figure 24. Comparison to intercooler and precooler solutions for problems with $\bar{C}_w^* > 5$.

The next graph in **Figure 25** from the paper looks at the influence of the R^* parameter for the same case – where $\frac{\dot{C}_{min}}{\dot{C}_{max}} = 0$, and the faster responses associated with larger values of R^* are shown.

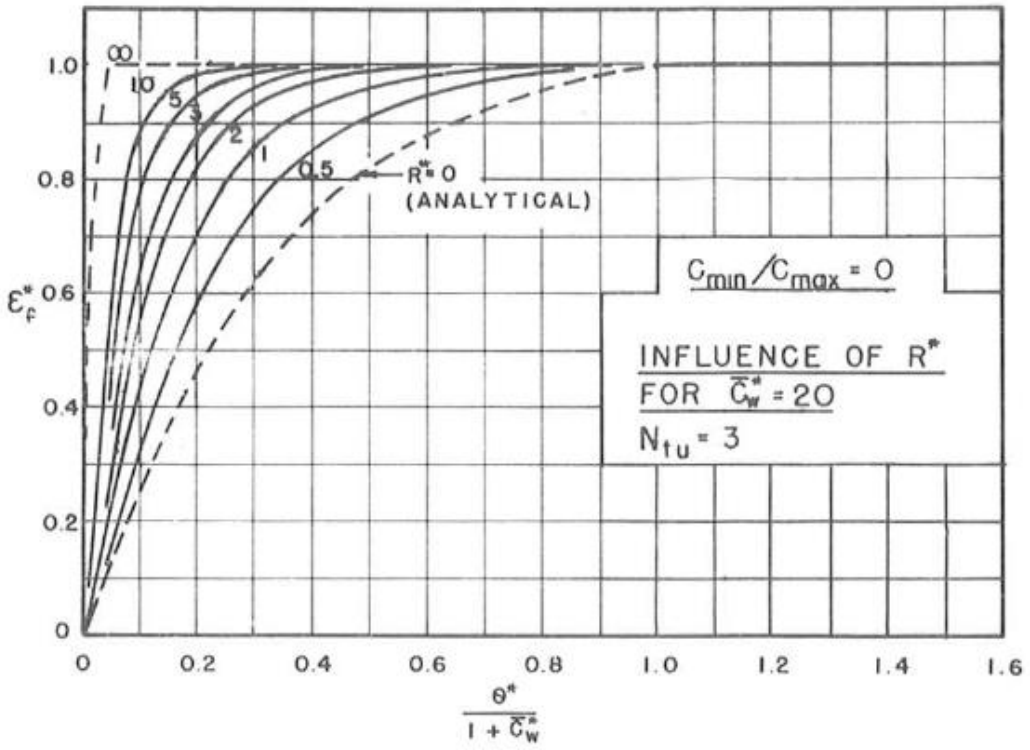

Figure 25. $\dot{C}_{min}/\dot{C}_{max} = 0$ solution, influence of R^* [2].

The numerical model shows a strong agreement to the analytical solution and electromechanical analog test results in **Figure 26**.

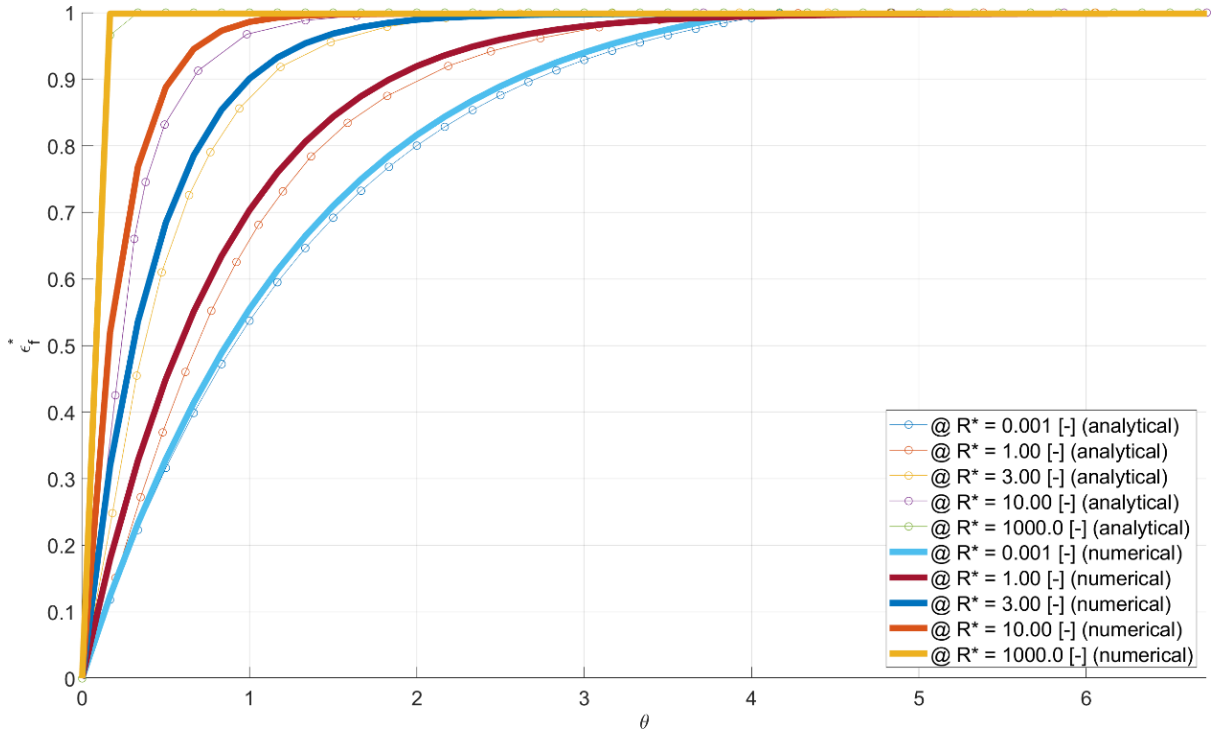

Figure 26. $\dot{C}_{min}/\dot{C}_{max} = 0$ solution, influence of R^*.

The final comparison looks at the following graph for the regenerator solutions for the case where $\bar{C}_w^* > 10$, $\dot{C}_{min}/\dot{C}_{max} = 1$, and $R^* = 1$. The model uses $\bar{C}_w^* = 1e6$ $[-]$ to solve.

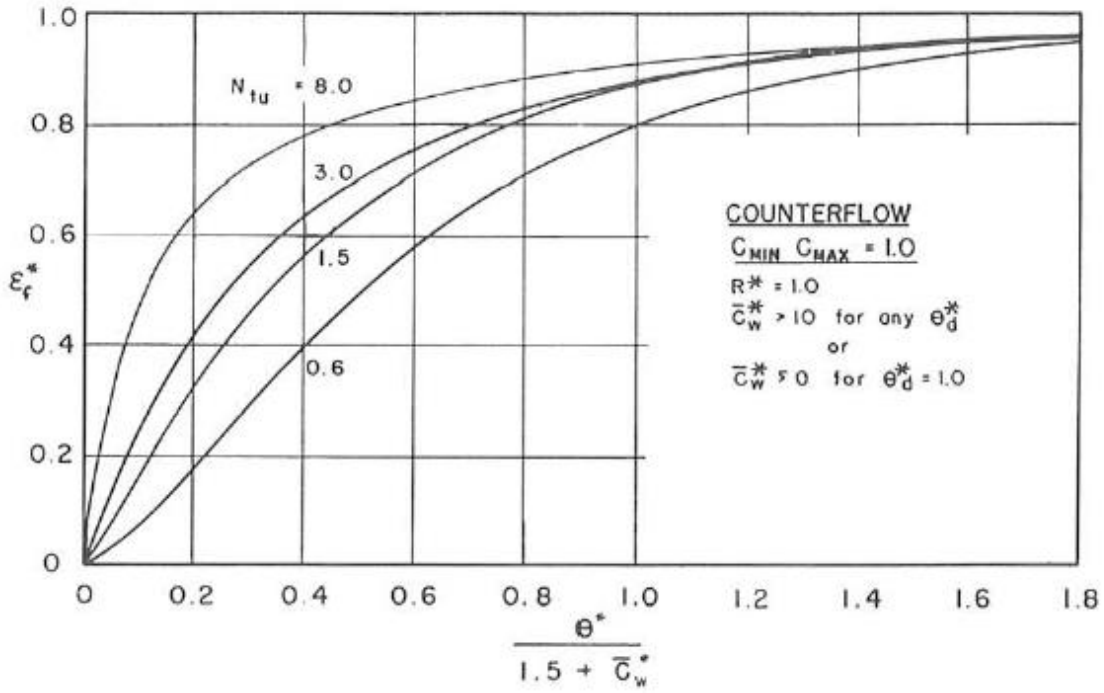

Figure 27. Regenerator solution for problems with $\bar{C}_w^* > 10$ [2].

There is a clear correlation shown by the graphs in **Figure 28**; however, values most closely match at high values of NTU. Because NTU is a proportionate to the overall thermal conductance UA and inversely proportional to the minimum capacitance rate $\dot{C}_{min}$, heat is transferred very efficiently at high values of NTU. Source [2] also points out that data at $NTU = 8$ was obtained from a computer program due to excessive error in solutions from the electromechanical lumped-parameter analog results when $NTU > 3$ at $C_R = 1$.

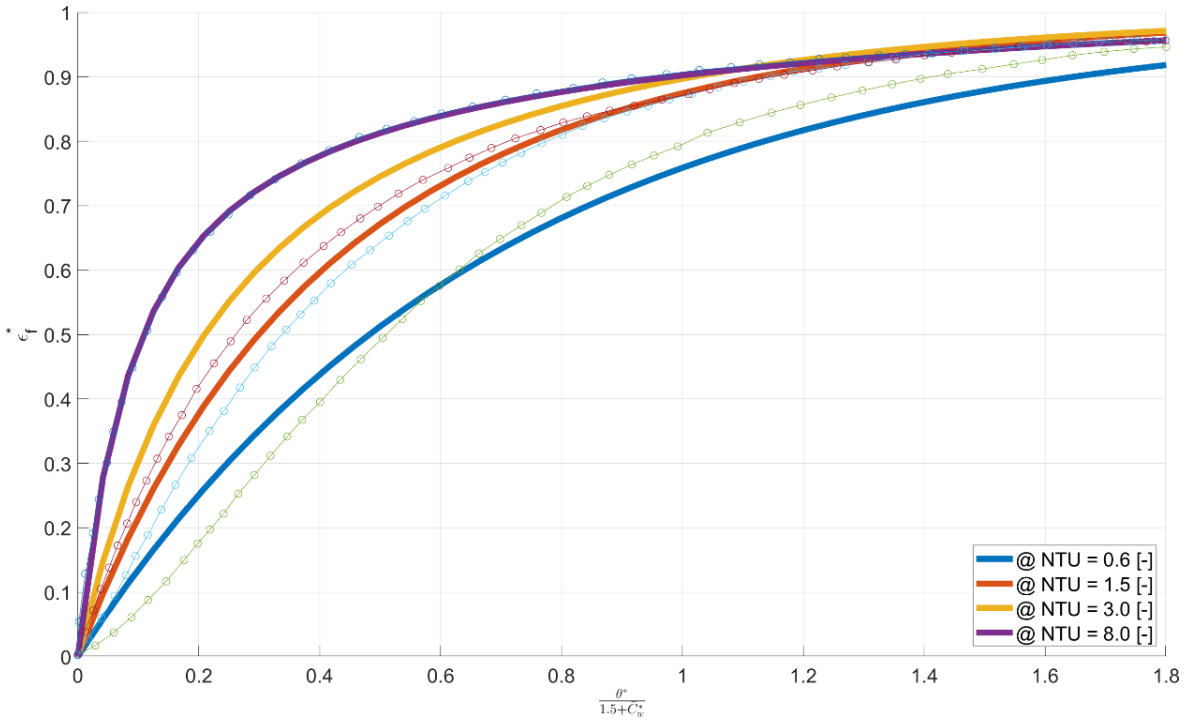

Figure 28. Comparison for regenerator solution for problems with $\bar{C}_w^* > 10$.

3.5 Model for Ramped Fluid Inlet Properties

This model takes inputs for both the hot and cold flow inlet conditions as a function of time. The user can either create a new function that details inlet conditions or use the existing inlet functions as a baseline. To demonstrate model functionality for ramped conditions, key graphs are compared for varied inputs and simulation conditions for the solution are presented. This is important to consider in the context of start-up for a high-temperature power cycle. First, a capacitance ratio of 0.5 will be examined, then an unbalanced condition in the case of a boiler and then a balanced condition in the case of a recuperator.

3.5.1 Simulation Conditions

The inputs are specified in **Table 4** for the first set of graphs in the model demonstration section.

Table 4. Simulation Conditions for Ramped Inputs

Property	Value	Units	Property	Value	Units	Property	Value	Units
UA_h	40	[W/K]	$T_{h,in,ini}$	300	[K]	$T_{h,in,fin}$	875	[K]
UA_c	40	[W/K]	$T_{c,in,ini}$	300	[K]	$T_{c,in,fin}$	375	[K]
C_{tot}	80	[J/K]	$\dot{C}_{h,in,ini}$	10	[W/K]	$\dot{C}_{h,in,fin}$	20	[W/K]
$R_{cond,tot}$	1	[K/W]	$\dot{C}_{c,in,ini}$	20	[W/K]	$\dot{C}_{c,in,fin}$	40	[W/K]
τ	C_{tot}/UA	[s]	$\beta_{T_{h,in}}$	25	[K/s]	$\beta_{\dot{C}_{h,in}}$	1	[W/Ks]
t_{sim}	10τ	[s]	$\beta_{T_{c,in}}$	5	[K/s]	$\beta_{\dot{C}_{c,in}}$	2	[W/Ks]
t_{span}	$0 \dots t_{sim}$	[s]	$T_{m,ini}$	300	[K]			
N	101	[-]	C_R	0, 0.5, 1	[-]			
M	121	[-]						

The ramping rates, β, result in changing values of the fluid inlet properties throughout simulation – meaning there is ramping in the fluid inlet parameters unlike in the previous graphs. Users may specify desired ramp rates, and the function will return this value for each timestep to the integration function.

Because ramping has been introduced, the ramp time must also be considered – this value is calculated inside the inlet functions and is found in the main program by calling the function for the final timestep, M. It is required that none of the ramp times exceed the simulation time, t_{sim}. For the specified inputs:

Table 5. Inlet Property Ramp Times at C_R = 0.5

Property	Value	Units	Property	Value	Units
$t_{ramp,T_{h,in}}$	23	[s]	$t_{ramp,\dot{C}_{h,in}}$	10	[s]
$t_{ramp,T_{c,in}}$	15	[s]	$t_{ramp,\dot{C}_{c,in}}$	10	[s]

3.5.2 Model Demonstration

The following graphs in **Figure 29-37** display the three key graphs from section 3.3 – first, looking at the temperature profiles for the hot flow, cold flow, and metal, second, looking at the metal

temperatures at each position for a specified set of timesteps, and third, looking at the metal temperature response as a function of time for each specified position.

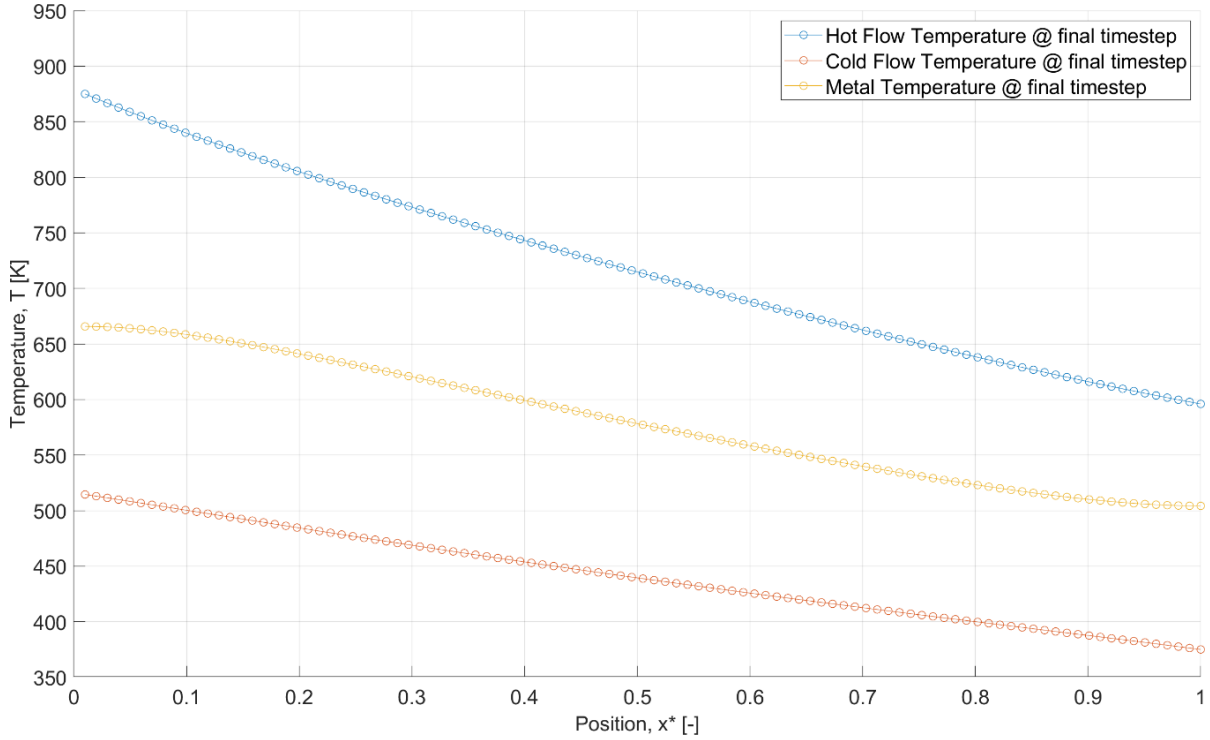

Figure 29. Temperature profiles for hot flow, cold flow, and metal at $C_R = 0.5\ [-]$.

As shown in **Figure 29**, the hot flow temperature undergoes a larger temperature change through the heat exchanger than the cold flow at the final timestep M. This results in final outlet temperatures of $T_{h,out} \cong 596\ [K]$ and $T_{c,out} \cong 514.5\ [K]$ and an effectiveness of $\varepsilon_{fin} \cong 0.558\ [-]$. This is very close to the steady-state effectiveness, from the effectiveness-NTU model, of $\varepsilon_{fin,ss} = 0.565\ [-]$, and if $R_{cond,tot} = 1e6\ [K/W]$, then $\varepsilon_{fin} \cong 0.565\ [-]$, matching the effectiveness-NTU model exactly. The metal temperatures at node 1 and N are $T_{m,1} \cong 666\ [K]$ and $T_{m,N} = 504.5\ [K]$, respectively.

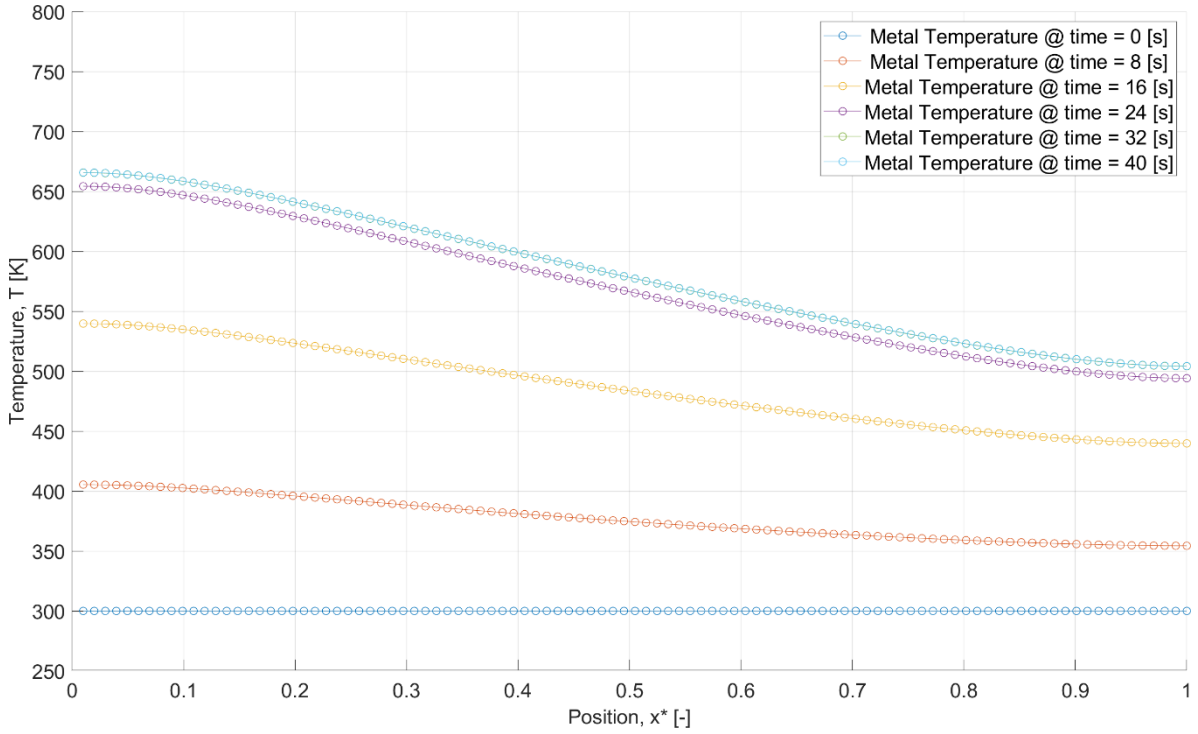

Figure 30. Metal temperature profiles at $C_R = 0.5\ [-]$.

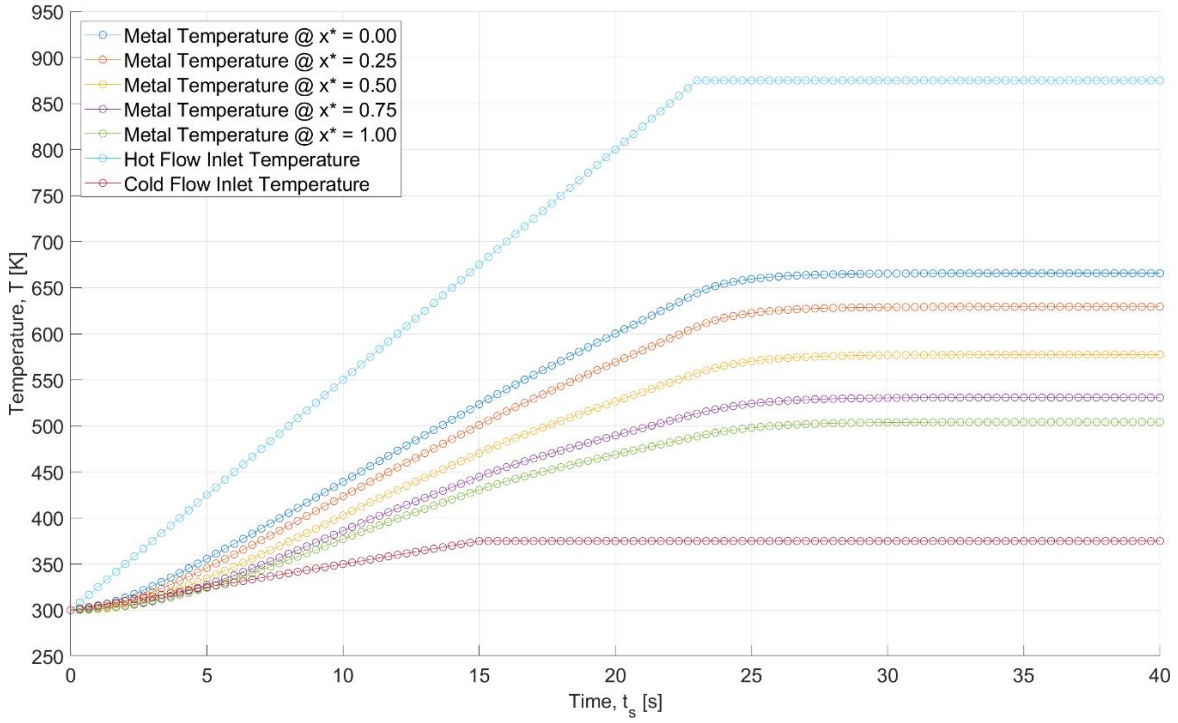

Figure 31. Metal temperature time response at $C_R = 0.5\ [-]$.

Then, for the unbalanced condition in the case of a boiler, the initial and final capacitance rate of the cold fluid is increased to $\dot{C}_{c,in,ini} = 2000\ [W/K]$ and $\dot{C}_{c,in,fin} = 4000\ [W/K]$. This results in a capacitance ratio of $C_R = 0.005 \approx 0\ [-]$. To maintain an equal ramp time between the hot and cold fluids, the ramp rate of the cold fluid capacitance rate is increased to $\beta_{\dot{C}_{c,in}} = 200\ [W/Ks]$.

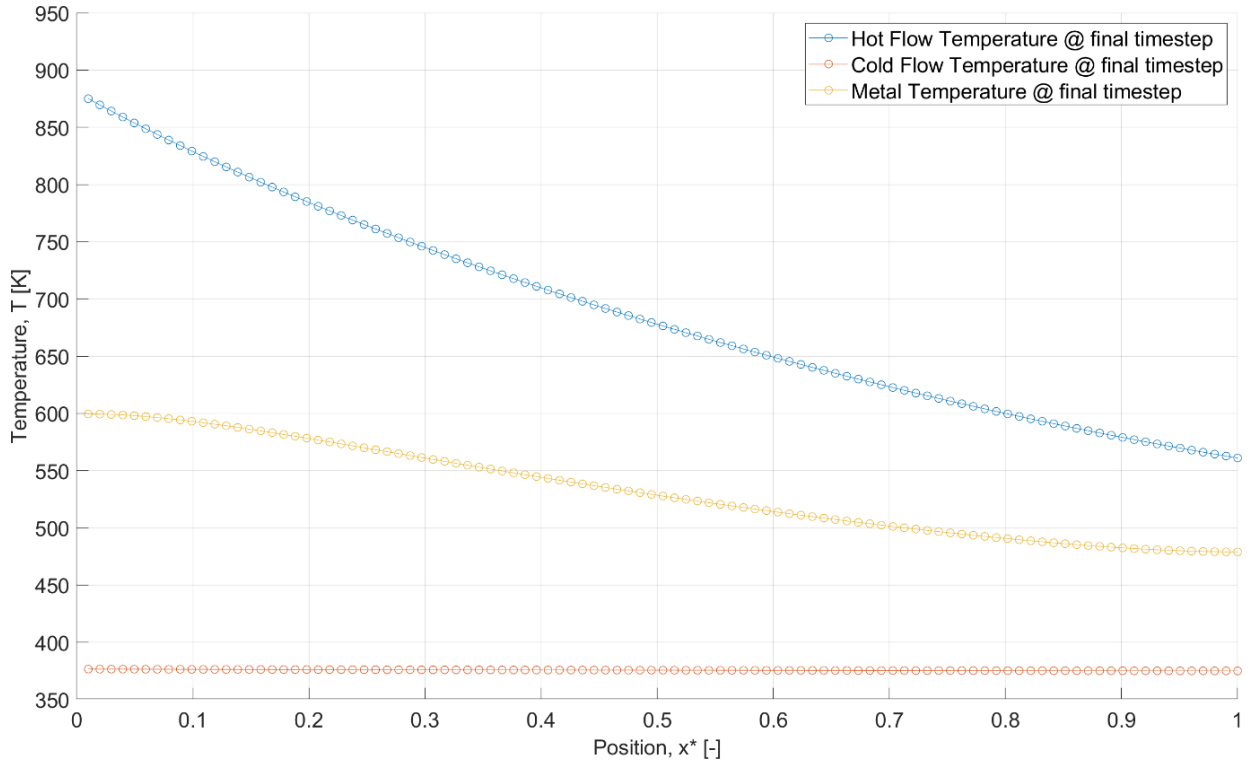

Figure 32. Temperature profiles for hot flow, cold flow, and metal at $C_R \approx 0\ [-]$.

As shown in **Figure 32**, the cold flow temperature is constant at the final timestep M. This results in final outlet temperatures of $T_{h,out} \cong 561\ [K]$ and $T_{c,out} \cong 377\ [K]$ and an effectiveness of $\varepsilon_{fin} \cong 0.628\ [-]$. This is very close to the steady-state effectiveness, from the effectiveness-NTU model, of $\varepsilon_{fin,ss} = 0.631\ [-]$, and if $R_{cond,tot} = 1e6\ [K/W]$, then $\varepsilon_{fin} \cong 0.631\ [-]$, matching the effectiveness-NTU model exactly. The metal temperatures at node 1 and N are $T_{m,1} \cong 599\ [K]$ and $T_{m,N} = 479\ [K]$, respectively.

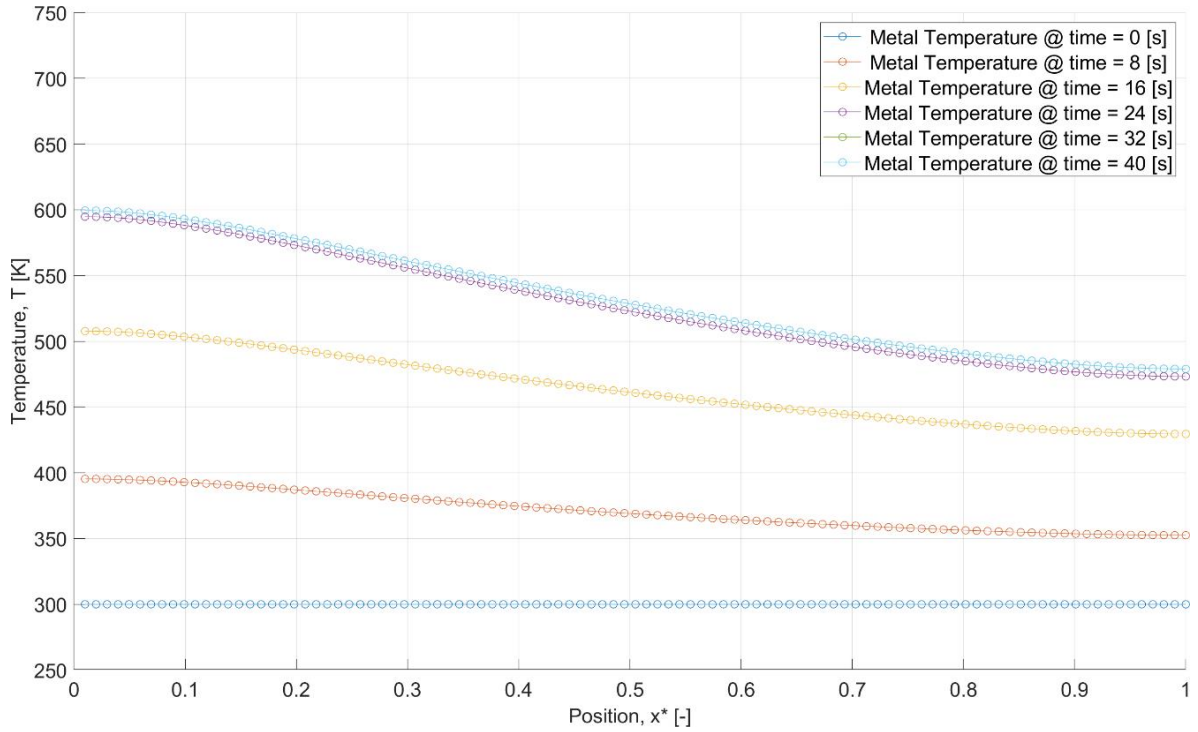

Figure 33. Metal temperature profiles at $C_R \approx 0\ [-]$.

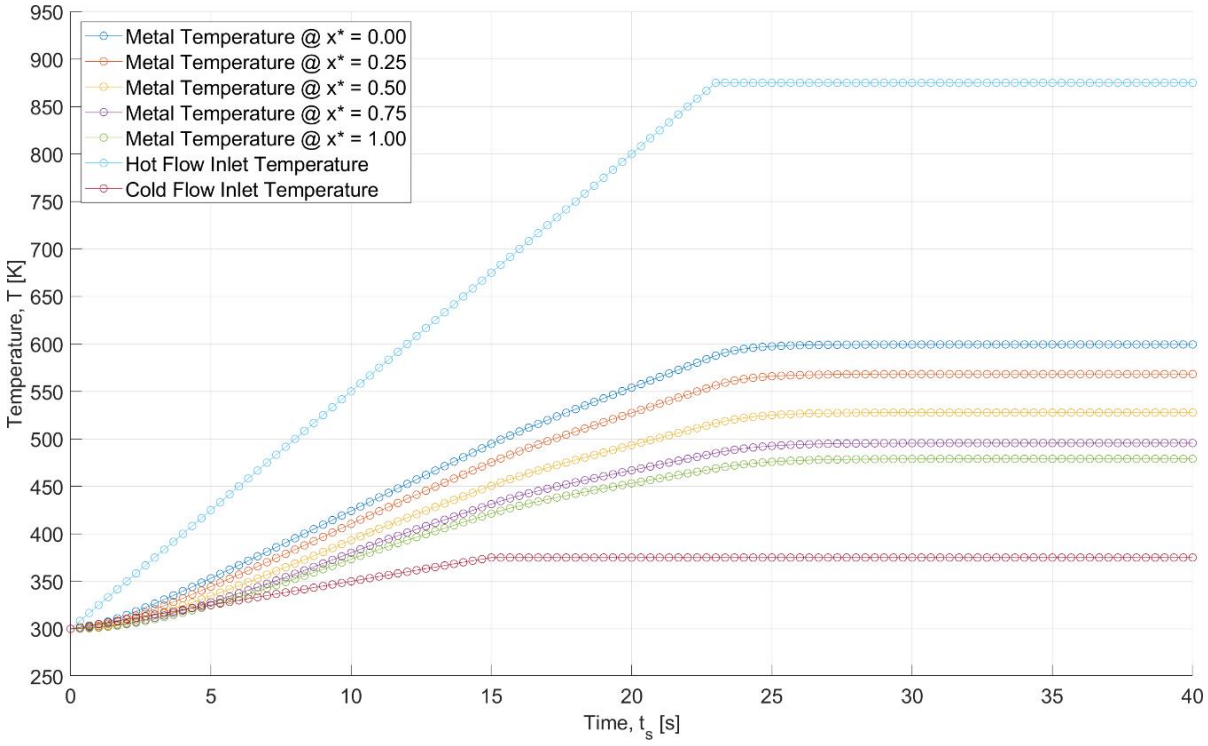

Figure 34. Metal temperature time response at $C_R \approx 0\ [-]$.

Figure 34 shows interesting behavior 10 and 15 seconds where the capacitance rate of both fluids has finished ramping, the cold fluid inlet temperature is almost done ramping, and the hot inlet temperature is still ramping. There is the most significant disturbance in the linear trend of the metal temperatures at points closest to the hot outlet and cold inlet of the heat exchanger.

Then, for the balanced condition in the case of a perfectly balanced recuperator, the initial and final capacitance rate of the cold fluid is increased to $\dot{C}_{c,in,ini} = 10\ [W/K]$ and $\dot{C}_{c,in,fin} = 20\ [W/K]$. This results in a capacitance ratio of $C_R = 1\ [-]$. To maintain an equal ramp time between the hot and cold fluids, the ramp rate of the cold fluid capacitance rate is decreased to $\beta_{\dot{C}_{c,in}} = 1\ [W/Ks]$.

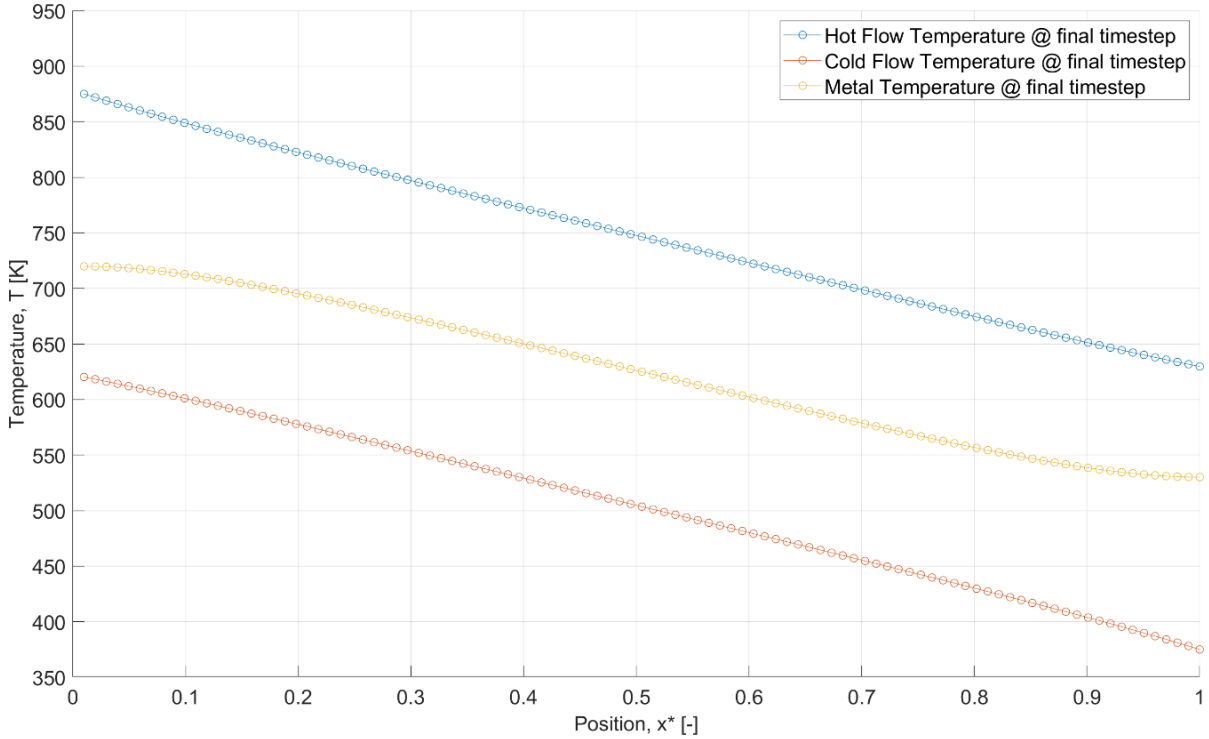

Figure 35. Temperature profiles for hot flow, cold flow, and metal at $C_R = 1\ [-]$.

As shown in **Figure 35**, the cold flow temperature undergoes a larger temperature change through the heat exchanger than the hot flow at the final timestep M. This results in final outlet

temperatures of $T_{h,out} \cong 630\ [K]$ and $T_{c,out} \cong 620\ [K]$ and an effectiveness of $\varepsilon_{fin} \cong 0.491\ [-]$. This is very close to the steady-state effectiveness, from the effectiveness-NTU model, of $\varepsilon_{fin,ss} = 0.5\ [-]$, and if $R_{cond,tot} = 1e6\ [K/W]$, then $\varepsilon_{fin} \cong 0.5\ [-]$, matching the effectiveness-NTU model exactly. The metal temperatures at node 1 and N are $T_{m,1} \cong 720\ [K]$ and $T_{m,N} = 530\ [K]$, respectively.

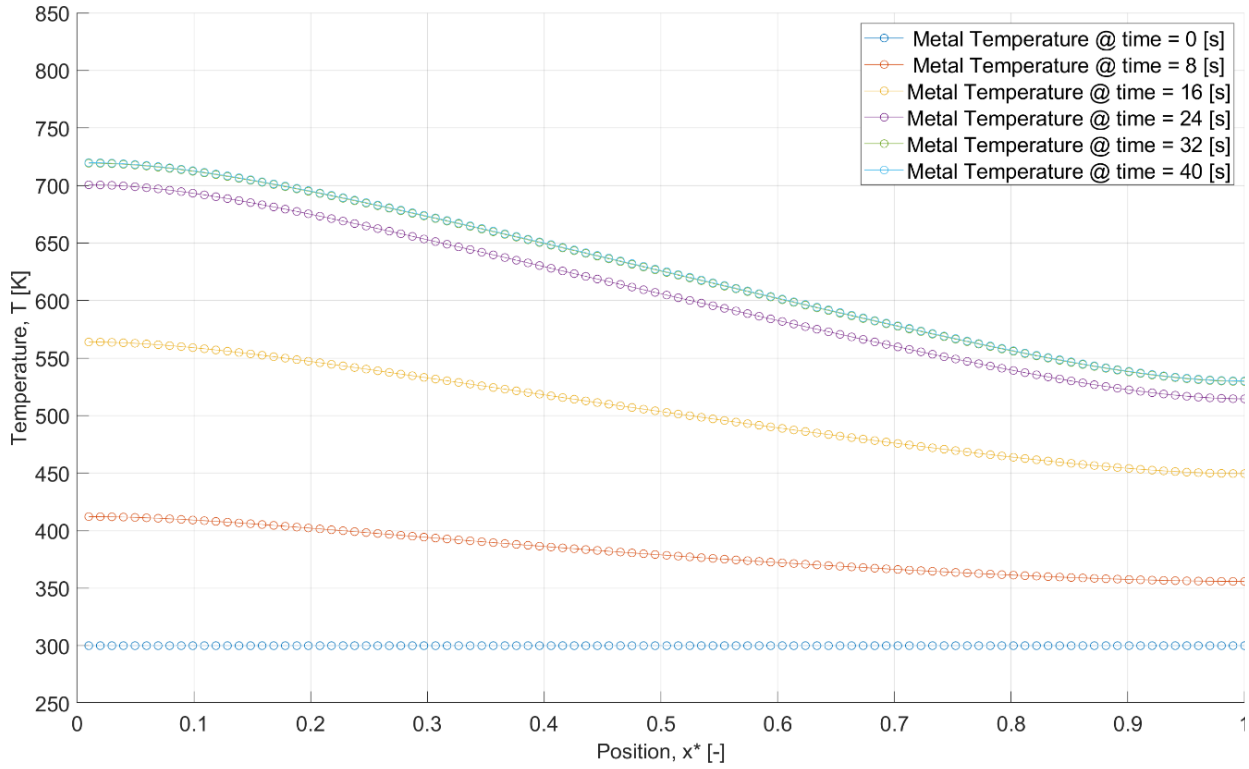

Figure 36. Metal temperature profiles at $C_R = 1\ [-]$.

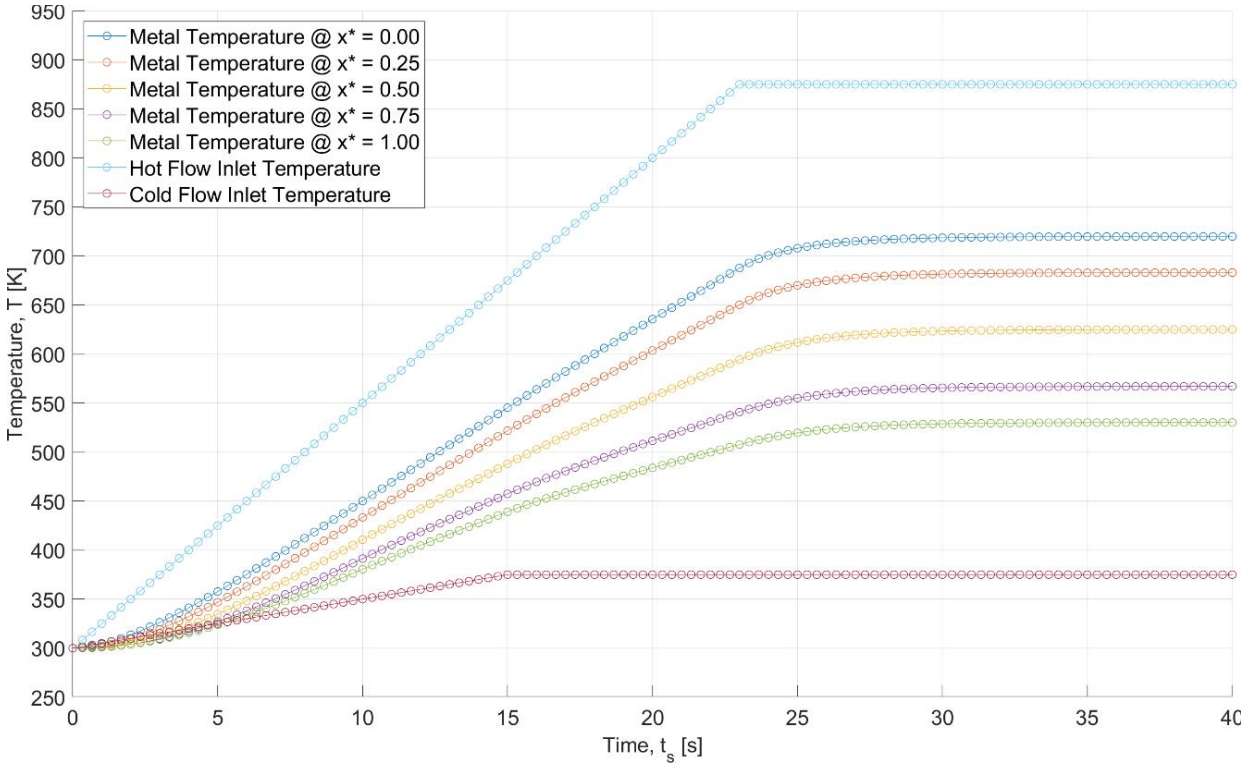

Figure 37. Metal temperature time response at $C_R = 1\ [-]$.

The following table summarizes the values from each of the previous three cases. The table shows an increase in the fluid outlet temperatures as well as the metal inlet and outlet temperatures as capacitance ratio increases; however, a decrease in the heat exchanger effectiveness is observed over the same increase in capacitance ratios.

Table 6. Response to Varied Capacitance Ratios

	C_R [-]		
Response	0	0.5	1
$T_{h,out}$	561.0	596.0	630.0
$T_{c,out}$	377.0	514.5	620.0
ε_{fin}	0.628	0.558	0.491
$T_{m,1}$	599.0	666.0	720.0
$T_{m,N}$	479.0	504.5	530.0

4 Model Deployment

The existing version of the code that runs this model is implemented in MATLAB. The files and an accompanying markdown file explaining the code can be found at the github address: https://github.com/uw-esolab/transient-hx. There are four distinct files required to operate this model:

i. CF_HXER_MODEL_v0

ii. CF_HXER_DTMDT_v0

iii. CF_HXER_HOT_INLET_v0

iv. CF_HXER_COLD_INLET_v0

4.1 CF_HXER_MODEL_v0

The first file contains the main body of the code, which calls the other three functions. This file requires inputs for the following values:

- Thermal conductance on hot-flow side, UA_h $[W/K]$: constant
- Thermal conductance on cold-flow side, UA_c $[W/K]$: constant
- Total heat capacity of metal (thermal mass), C_{tot} $[J/K]$: constant
- Total axial conduction resistance of metal, $R_{cond,tot}$ $[K/W]$: constant
- Initial temperature of metal nodes, $T_{m,ini}$ $[K]$: constant
- Number of nodes, N $[-]$: constant
- Number of timesteps, M $[-]$: constant
- Simulation time, t_{sim} $[s]$: constant, recommended 5 to 10 times multiple of time constant, τ

Then, the second file, CF_HXER_DTMDT_v0, is called using the specified inputs to integrate forward through time using MATLAB's built-in ODE45 solver – which evaluates the state equation by integrating through time for each node in the axial direction. Because this occurs in a function, the next step is to call that function to return the specified values for each node and timestep to the main code. After this has been done, the user will look to draw various conclusions from these values. As the code exists now, the following important values are examined:

- Metal temperature at inlet and outlet for final timestep
- Fluid inlet and outlet temperatures at final timestep
- Fluid inlet arrays for inlet temperatures and capacitance rates at each timestep
- Ramp times for fluid inlet temperatures and capacitance rates
- Temperature differentials across the heat exchanger for the inlet and outlet at all timesteps
- Minimum and maximum capacitance rates at each timestep
- Capacitance ratio at each timestep
- Heat exchanger sizing, NTU, at final timestep
- Actual heat transfer rates for hot and cold fluids at each timestep
- Maximum heat transfer rate at each timestep
- Heat exchanger effectiveness calculations for each timestep
- Effectiveness-NTU calculations for final timestep at steady-state for model confirmation

There are three primary graphs existing in the main body.

1. Metal temperatures at specified node for all timesteps, plotted temperature vs. simulation time
2. Metal temperatures at specified timestep for all nodes, plotted temperature vs. node position
3. Temperature profiles at final timestep for all nodes, plotted temperature vs. node position

Based on the user's inputs, each specified timestep may be altered in both the plot command line as well as in the legend command. Additionally, the user may alter the axes as needed. Each figure is currently automatically sized to be the full-size of the user's screen and a font-size of 16 is used. The figure size has been chosen this way to allow for the user to easily save each graph with a distinct file name to the working directory. The final two lines in each graph code block may be commented out to avoid saving every time the code is run. These are the lines starting with *saveas* and *export_fig*. Additional graphs may be added as needed to perform various analyses and/or verifications.

4.2 CF_HXER_DTMDT_v0

The second file contains the energy balances to be integrated in the finding of the complete temperature profiles. There are no required inputs for this file, and it can be left completely alone by the user. The first calculation performed in this function is the equal split of the total axial conduction resistance in the metal. Then, each energy balance is performed to find the temperature profiles, starting with the hot flow, then going to the cold flow, then finally, the metal nodes. It is important to note that the capacitance rate for the inlet has been assumed to

be constant throughout the heat exchanger – meaning the capacitance rate of each flow is the same at the fluid inlet and outlet.

4.3 CF_HXER_HOT_INLET_v0

The third file allows the user to specify the hot inlet properties for the temperature and capacitance rate for each timestep in the main body – for a total of M timesteps. Depending on the application the user has chosen, this file requires different inputs. By setting the variable, $condition$, equal to a value of 1, 2, or 3, the option will automatically be selected. For options where a non-constant value is provided for the inlet conditions, it is recommended that the time taken for this change to occur is less than the simulation time in the main window. This will allow the model to reach steady-state within the specified simulation time. The following options are available for the user:

1. Constant hot inlet properties
2. Ramped hot inlet properties
3. Alternatively specified hot inlet properties

For the first option – constant hot inlet properties – the user is required to input the following values:

- Hot inlet temperature, $T_{h,in}\ [K]$
- Hot inlet capacitance rate, $\dot{C}_{h,in}\ [W/K]$
- Hot inlet temperature total ramp time, $t_{ramp_{T_{h,in}}} = 0\ [s]$
- Hot inlet capacitance rate total ramp time, $t_{ramp_{\dot{C}_{h,in}}} = 0\ [s]$

For the second option – ramped hot inlet properties – the user is required to input the following values:

- Hot inlet temperature ramp rate, $\beta_{T_{h,in}}\ [K/s]$
- Hot inlet initial temperature, $T_{h,in,ini}\ [K]$
- Hot inlet final temperature, $T_{h,in,fin}\ [K]$
- Hot inlet capacitance rate ramp rate, $\beta_{\dot{C}_{h,in}}\ [W/Ks]$
- Hot inlet initial capacitance rate, $\dot{C}_{h,in,ini}\ [W/K]$
- Hot inlet final capacitance rate, $\dot{C}_{h,in,fin}\ [W/K]$

In turn, the function will return each of these values to the second file, CF_HXER_DTMDT_v0, for each timestep, M. Additionally, this file for the hot inlet properties can be called from the main code to find the ramp times for each specified property.

- Hot inlet temperature total ramp time, $t_{ramp_{T_{h,in}}}\ [s]$
- Hot inlet capacitance rate total ramp time, $t_{ramp_{\dot{C}_{h,in}}}\ [s]$

For the third option – alternatively specified hot inlet properties – it is entirely up to the user how to specify the variance in the inlet conditions as a function of time. If the user were to select something like a step input, then variables should be modified in the function return to specify the proper return times to the main window. There is code in the main window that calls this function that would also need to be modified to reflect the new return variables.

4.4 CF_HXER_COLD_INLET_v0

The fourth file allows the user to specify the cold inlet properties for the temperature and capacitance rate for each timestep in the main body – for a total of M timesteps. Depending on the application the user has chosen, this file requires different inputs. By setting the variable, $condition$, equal to a value of 1, 2, or 3, the option will automatically be selected. For options where a non-constant value is provided for the inlet conditions, it is recommended that the time taken for this change to occur is less than the simulation time in the main window. This will allow the model to reach steady-state within the specified simulation time. The following options are available for the user:

1. Constant cold inlet properties
2. Ramped cold inlet properties
3. Alternatively specified cold inlet properties

For the first option – constant cold inlet properties – the user is required to input the following values:

- Cold inlet temperature, $T_{c,in}$ $[K]$
- Cold inlet capacitance rate, $\dot{C}_{c,in}$ $[W/K]$
- Cold inlet temperature total ramp time, $t_{ramp_{T_{c,in}}} = 0$ $[s]$
- Cold inlet capacitance rate total ramp time, $t_{ramp_{\dot{C}_{c,in}}} = 0$ $[s]$

For the second option – ramped cold inlet properties – the user is required to input the following values:

- Cold inlet temperature ramp rate, $\beta_{T_{c,in}}$ $[K/s]$
- Cold inlet initial temperature, $T_{c,in,ini}$ $[K]$
- Cold inlet final temperature, $T_{c,in,fin}$ $[K]$
- Cold inlet capacitance rate ramp rate, $\beta_{\dot{C}_{c,in}}$ $[W/Ks]$
- Cold inlet initial capacitance rate, $\dot{C}_{c,in,ini}$ $[W/K]$
- Cold inlet final capacitance rate, $\dot{C}_{c,in,fin}$ $[W/K]$

In turn, the function will return each of these values to the second file, CF_HXER_DTMDT_v0, for each timestep, M. Additionally, this file for the cold inlet properties can be called from the main code to find the ramp times for each specified property.

- Cold inlet temperature total ramp time, $t_{ramp_{T_{c,in}}}$ $[s]$
- Cold inlet capacitance rate total ramp time, $t_{ramp_{\dot{C}_{c,in}}}$ $[s]$

For the third option – alternatively specified cold inlet properties – it is entirely up to the user how to specify the variance in the inlet conditions as a function of time. If the user were to select something like a step input, then variables should be modified in the function return to specify the proper return times to the main window. There is code in the main window that calls this function that would also need to be modified to reflect the new return variables.

Additionally, the user may create their own function file with time as the only input titled as specified for the hot and cold fluid inlet properties. This allows for the user to create an entirely new function and run the model without ever opening the code described in this thesis.

5 Conclusion

5.1 Summary

A model has been created for a transient counterflow plate heat exchanger with axial conduction in the separating wall between the fluids. This model can be used in various situations requiring a counterflow heat exchanger. For example, one especially relevant application is the modeling of cycle start-up in high-temperature power cycle applications. The model has been verified against multiple types of transient simulations from different authors in addition to verification against the conventional effectiveness-NTU model at steady-state. This model is useful when looking at a more detailed analysis of what is actually happening within the heat exchanger when non-steady-state conditions exist. Another advantage of this model is that it is not so complicated that users are unable to draw useful conclusions without the knowledge of advanced power cycle characteristics, complex heat exchanger geometry, and complicated fluid properties.

5.2 Future Work

This model would be useful in making comparisons to experimental work. A great example would be one that includes a heat exchanger material that may be 3D printed with properties such as conductivity specified by the manufacturer. For cycle start-up, the outputs of this model could be either compared to experimental results or used as a precursor to analyze anticipated behavior given the properties of the actual heat exchanger and fluids. In addition to some possible model improvements relating to accuracy, users may also include more graphs of interest. It would be really interesting to see this model expanded to calculate specific properties of fluids from a property library, although that was deemed unnecessary for the purpose of this

model at this time. It would also be interesting to compare the outputs of this model to a computationally intensive and hyper-focused model like NPSS [3]. A comparison to a unit-step increase in the inlet temperatures as shown by F. E. Romie [5] could serve as a useful 3rd condition for inlet properties as specified in sections 4.3 and 4.4.

While some users may be content with the tabulated outputs for each variable in MATLAB, there may also be a way to streamline the connection between this model and another model housed outside of MATLAB. For a user modeling each component in a specified cycle, this model may be more useful if it was housed entirely in a different solver. However, MATLAB's ODE45 solver is implemented, so the integration technique would have to be modified in a different solver. This model has value in providing improved characterization of counterflow heat exchangers within an operating power cycle undergoing transient conditions, and the effects of that behavior may lead to a better understanding of the effects on other cycle componentry. Additional model verification using experimental data would be beneficial, as well.

6 References

[1] C. S. Turchi, Z. Ma, T. W. Neises, and M. J. Wagner, "Thermodynamic Study of Advanced Supercritical Carbon Dioxide Power Cycles for Concentrating Solar Power Systems," *Journal of Solar Energy Engineering, ASME*, vol. 135, no. 4, pp. 1–7, 2013, doi: 10.1115/1.4024030.

[2] A. L. London, F. R. Biancardi, and J.W. Mitchell, "The Transient Response of Gas-Turbine-Plant Heat Exchangers — Regenerators, Intercoolers, Precoolers, and Ducting," *Journal of Engineering for Power, ASME,* 1959.

[3] C. J. Tang, A. McClung, D. Hofer, and M. Huang, "Transient Modeling of 10 MW Supercritical CO2 Brayton Power Cycles using Numerical Propulsion System Simulation (NPSS)," *Proceedings of ASME Turbo Expo 2019*, vol. 9, pp. 1–10, 2019, doi: 10.1115/GT2019-91443.

[4] P. Wu, C. Gao, and J. Shan, "Development and Verification of a Transient Analysis Tool for Reactor System using Supercritical CO2 Brayton Cycle as Power Conversion System," *Science and Technology of Nuclear Installations*, vol. 2018, 2018, doi: 10.1155/2018/6801736.

[5] F. E. Romie, "Transient Response of the Counterflow Heat Exchanger," *Journal of Heat Transfer*, vol. 106, pp. 620-626, 1984, doi: 10.1115/1.3247489.

[6] G. F. Nellis and S. A. Klein, *Heat Transfer,* New York, NY: Cambridge University Press, 2009.

[7] M. J. Wagner, A. M. Newman, W. T. Hamilton, and R. J. Braun, "*Optimized Dispatch in a First-Principles Concentrating Solar Power Production Model,*" *Applied Energy*, vol. 203, pp. 959–971, 2017, doi: 10.1016/j.apenergy.2017.06.072.

[8] W. T. Hamilton, M. A. Husted, A. M. Newman, R. J. Braun, and M. J. Wagner, "*Dispatch Optimization of Concentrating Solar Power with Utility-Scale Photovoltaics*," *Optimization and Engineering,* vol. 21, pp. 335-369, 2019, doi: 10.1007/s11081-019-09449-y.